Publications of the Astronomical Society of Australia (2025), **42**, e003, 17 pages
doi:10.1017/pasa.2024.114

Research Article

The fast radio burst population energy distribution

Wayne R. Arcus[1], Clancy James[1], Ron Ekers[2,1], Jean-Pierre Macquart[1], Elaine Sadler[3,2], Randall B. Wayth[1], Keith Bannister[2,3], Adam T. Deller[4], Chris Flynn[4], Marcin Glowacki[1], Alexa Gordon[5,6], Lachlan Marnoch[7,8,2,9], Stuart Ryder[7] and Ryan M. Shannon[4]

[1]International Centre for Radio Astronomy Research, Curtin University, Perth, WA, Australia, [2]Australia Telescope National Facility, CSIRO, Space and Astronomy, Epping, NSW, Australia, [3]Sydney Institute for Astronomy, School of Physics A28, The University of Sydney, Sydney, NSW, Australia, [4]Centre for Astrophysics and Supercomputing, Swinburne University of Technology, Hawthorn, VIC, Australia, [5]Center for Interdisciplinary Exploration and Research in Astrophysics (CIERA), Northwestern University, Evanston, IL, USA, [6]Department of Physics and Astronomy, Northwestern University, Evanston, IL, USA, [7]School of Mathematical and Physical Sciences, Macquarie University, Sydney, NSW, Australia, [8]Astrophysics and Space Technologies Research Centre, Macquarie University, Sydney, NSW, Australia and [9]ARC Centre of Excellence for All-Sky Astrophysics in 3 Dimensions (ASTRO 3D), Australia

Abstract

We examine the energy distribution of the fast radio burst (FRB) population using a well-defined sample of 63 FRBs from the Australian Square Kilometre Array Pathfinder (ASKAP) radio telescope, 28 of which are localised to a host galaxy. We apply the luminosity-volume (V/V_{max}) test to examine the distribution of these transient sources, accounting for cosmological and instrumental effects, and determine the energy distribution for the sampled population over the redshift range $0.01 \lesssim z \lesssim 1.02$. We find the distribution between 10^{23} and 10^{26} J Hz^{-1} to be consistent with both a pure power-law with differential slope $\gamma = -1.96 \pm 0.15$, and a Schechter function with $\gamma = -1.82 \pm 0.12$ and downturn energy $E_{\mathrm{max}} \sim 6.3 \times 10^{25}$ J Hz^{-1}. We identify systematic effects which currently limit our ability to probe the luminosity function outside this range and give a prescription for their treatment. Finally, we find that with the current dataset, we are unable to distinguish between the evolutionary and spectral models considered in this work.

Keywords: Radio continuum: transients; methods: data analysis; surveys; cosmology: miscellaneous; transients: fast radio bursts

(Received 16 August 2024; revised 3 November 2024; accepted 8 November 2024)

1. Introduction

Fast radio bursts (FRBs) are short duration (millisecond timescale), dispersed, transient events in the radio spectrum known to originate from cosmological distances (Lorimer et al. 2007; Thornton et al. 2013; Chatterjee et al. 2017; Bannister et al. 2019). Current research has two major directions: to determine their progenitor source(s) and to use them as cosmological probes (Macquart et al. 2020). Accordingly, the FRB population statistics continues to be a topic of considerable conjecture (see e.g. Petroff, Hessels, & Lorimer 2022, and references therein).

Determining the intrinsic energy distribution (i.e. luminosity function) of FRBs has, hitherto, proven to be problematic. The first impediment stems from radio telescopes with optics that make an accurate determination of the FRB location within the telescope beam difficult, such as Parkes/Murriyang (e.g. Thornton et al. 2013; Keane et al. 2018), UTMOST (Farah et al. 2019), FAST (Niu et al. 2021), and the first FRB searches with CHIME (CHIME/FRB Collaboration: Amiri et al. 2021). This complicates the construction of a fluence-complete sample and determining the effective survey area (see Keane & Petroff 2015; Macquart & Ekers 2018a). This issue is effectively mitigated when using telescope arrays to search for FRBs, as pioneered by the Australian Square Kilometre Array Pathfinder (ASKAP) telescope – which uses phased array feeds (PAFs) to provide a wide field of view (FoV) with dense coverage of the focal plane – permitting reliable estimates of the survey area and FRB fluences to be made (Bannister et al. 2017; Shannon et al. 2018). Even then, however, the relationship between a detected FRB's signal-to-noise (S/N) and its fluence is distorted by dispersion measure smearing, scattering, and the nuances of the particular detection algorithm. A significant literature is now dedicated to modelling these effects (Cordes & McLaughlin 2003; Keane & Petroff 2015; Qiu et al. 2023; Merryfield et al. 2023; Hoffmann et al. 2024a), allowing them to be accounted for in FRB energy determination.

The second impediment is the difficulty in obtaining an FRB distance estimate, which yields the FRB energy and survey volume. This requires either arcsecond-precision FRB localisations, thereby permitting the identification of the host galaxy, or the existence of a relation between the FRB dispersion measure, DM, and redshift, z. ASKAP has helped provide both, with a large sample of FRBs localised to their host galaxies (Shannon et al. 2024), and the establishment of a z-DM relationship, known as the Macquart Relation (Macquart et al. 2020). Other instruments with similar capabilities include DSA 110 (Law et al. 2024), MeerKAT (Rajwade et al. 2022), the VLA (Law et al. 2018), and CHIME's outriggers (Leung et al. 2021).

A great deal of literature has attempted to draw conclusions on the FRB luminosity function. Relatively few, however, have made a

Corresponding author: Wayne R. Arcus; Email: wayne.arcus@icrar.org

Cite this article: Arcus WR, James C, Ekers R, Macquart J-P, Sadler E, Wayth RB, Bannister K, Deller AT, Flynn C, Glowacki M, Gordon A, Marnoch L, Ryder S and Shannon RM. (2025) The fast radio burst population energy distribution. *Publications of the Astronomical Society of Australia* **42**, e003, 1–17. https://doi.org/10.1017/pasa.2024.114

proper account for the above-mentioned effects, as emphasised by Connor (2019) – examples include Luo et al. (2020), James et al. (2021a), Shin et al. (2023), Hoffmann et al. (2024b). However, these fits rely on assumptions about the functional form of the FRB energy distribution and source evolution, which may differ from that of other classes of transients. A non-parametric way to determine both – the $V/V_{\max}$ method – was described by Schmidt (1968), in the context of studies of the quasar population. The simplest application of this method is to test for a spatially uniform distribution of FRB sources, which has been applied to FRB data by several authors (Oppermann, Connor, & Pen 2016; Shannon et al. 2018; Locatelli et al. 2019). Others have applied the analysis determining the FRB energy distribution from non-localised FRBs (Lu & Piro 2019; Hashimoto et al. 2022; Zhang et al. 2024), which has the aforementioned uncertainties of fluctuations in the Macquart relation.

In this work, we update these analyses using FRBs detected by the Commensal Real-time ASKAP Fast Transients (CRAFT; Macquart et al. 2010) survey with ASKAP (Hotan et al. 2021). In particular, we use a large sample of FRBs with known redshift, allowing for the first time an accurate measurement of both V and $V_{\max}$ for FRBs. This allows unbiased estimates of their energy and spatial distributions to be used.

In Section 2 we review the volumetrics and formation of the energy distribution for a sample being analysed. We then apply the approach to the ASKAP sample and outline our results and observations in Section 3. In Section 4 we discuss the implications of the energy distributions and present our conclusions in Section 5.

2. The energy function

2.1 The $V/V_{\max}$ test

The discovery of FRBs in 2007 (Lorimer et al. 2007) has many similarities to the discovery of quasars (Schmidt 1963); both are new classes of extragalactic objects catalogued in surveys with well-defined but complex detection limits.

To estimate the spatial distribution and luminosity function of quasars (then referred to as QSOs), Schmidt (1968) introduced the $V/V_{\max}$ parameter which, for each source, provides a measure of its position within the maximum volume over which it would have been observed in the complete sample. Due to the uncertainty in cosmological models at the time, Schmidt (1968) calculated volumes in co-moving coordinates using two cosmological models: luminosity distance $D_L \propto z$, and $D_L \propto z(1+0.5z)$. Schmidt notes that $V/V_{\max}$ provides a very simple test of uniformity for the spatial distribution in a sensitivity-limited sample, with an expectation value $<+V/V_{\max}>=0.5$. In the case of quasars, $V/V_{\max}$ was found to be significantly larger than 0.5, and Schmidt concluded that the sample was strongly evolving. The expected uniformity in $V/V_{\max}$ was achieved by weighting the Cartesian volume $V \sim D_L^3$ by an assumed source evolution of $(1+D_L)^2$. Schmidt then estimated the local luminosity function by using $1/V_{\max}$ to weight the contribution to the spatial density from each source separately, and then grouped the sources in luminosity bins, wherein these luminosities were converted to the rest frequency.

Like quasars, FRBs are also cosmologically distributed, and the problems of analysing their redshift evolution and luminosity function are very similar. The $V/V_{\max}$ method requires a complete sample of sources above a well-defined flux (or fluence) limit. Even if the redshifts of these sources are unknown or poorly defined, the mean value of $V/V_{\max}$ can indicate whether the sources are distributed uniformly through the sample volume. A uniform distribution (with $<+V/V_{\max}>\approx 0.5$) implies a population that is non-evolving (i.e. not changing with distance) within the sample volume, while a larger or smaller value implies either an incompleteness in selection, or a population that undergoes some form of redshift evolution within the sample volume.

For a source population where redshift measurements are available for individual objects, and where there is also little or no evolution within the sample volume, a luminosity function can be calculated by summing the values of $1/V_{\max}$ within different luminosity bins. Local radio luminosity functions (RLFs) for large, complete samples have been calculated by several authors (e.g. Condon, Cotton, & Broderick 2002; Sadler et al. 2002; Best et al. 2005; Mauch & Sadler 2007), and Pracy et al. (2016) calculated the RLF for high- and low-excitation radio galaxies in several redshift bins out to $z \sim 0.75$. Avni & Bahcall (1980) extended Schmidt (1968)'s method to samples with different completeness limits in two (or more) different parameters; this technique may be used to measure a bivariate luminosity function, for example, a set of RLFs for different bins in optical luminosity (Mauch & Sadler 2007) or black hole mass determination (Best et al. 2005).

If the redshift range covered by a survey is large enough that redshift evolution occurs within the sample-volume (i.e. $V/V_{\max}$ has a value significantly different from 0.5), then this evolution must be taken into account. Examples from the literature include studies of the luminosity function of gamma-ray bursts (Schmidt 2009) and the redshift evolution of powerful radio galaxies (Dunlop & Peacock 1990).

Schmidt's methods may be applied directly to the FRB population, with a few significant differences. Since FRBs are transient rather than static sources of emission, the observing time should be included in the analysis as well as the survey area. Transients are typically characterised by their fluence and energy distribution rather than their flux and luminosity function. To keep notation consistent with Schmidt (1968), hereinafter we refer to FRB luminosities and their RLF when describing the distribution of their spectral energy density, E_ν. If the positions are not determined well enough during the outburst, the location in the FoV cannot be determined. Thus the sensitivity of the telescope beam at the detection point, hence the correction for that sensitivity, cannot be made. For the population of FRBs that have not been observed to repeat, only surveys which determine the position in the FoV can therefore be used – significantly reducing the applicable sample size.

First, we use the $V/V_{\max}$ test to check whether the FRBs in our sample are uniformly distributed in space. Then, following Schmidt, we use $1/V_{\max}$ for each FRB to estimate its contribution to the density of FRBs of that luminosity. The estimation of $V_{\max}$ is the critical aspect introduced by this analysis: for FRB surveys it can be applied on a per source basis, provided the survey detection limit, the detected S/N and the position in the FoV are known for each FRB. This requirement significantly limits the sample of FRBs that can be used, and we therefore confine our analysis to suitable FRBs from the CRAFT survey, which satisfy these criteria. We do this for FRBs with known host galaxies for which V and $V_{\max}$ can be calculated. We also investigate the effect of using DM as a distance proxy by comparing this result to that obtained when estimating FRB distances from their DMs using the cosmological DM-z ('Macquart') relation (Macquart et al. 2020). For simplicity,

https://doi.org/10.1017/pasa.2024.114 Published online by Cambridge University Press

in the main body of this work, we ignore FRB spectral dependence and source evolution; however, we consider both in Appendix A, and show that neither have a strong influence given current data. We do not explicitly calculate the time-dependence of the survey volume, thus we cannot calculate the FRB rate. Moreover, since we use data from both ASKAP's Fly's Eye and Incoherent Sum (ICS) modes in different proportions for the two samples, the relative normalisation is arbitrary. We discuss this further in Appendix B.

The ratio of volumes from which the FRB has been detected, V, to that in which it could have been detected, $V_{\max}$, is a measure of the position of the detected event within the probed volume. The statistic $\langle V/V_{\max}\rangle$ is the algebraic mean of events in a sample and is expressed as:

$$\langle V/V_{\max}\rangle = \frac{1}{N}\sum_{i=1}^{N}\frac{V_i}{V_{\max,i}}, \tag{1}$$

where i represents the i^{th} event in a sample of N events. A spatially uniform sample would be uniformly distributed over the range [0, 1] with $\langle V/V_{\max}\rangle = 0.5$ (Schmidt 1968). The luminosity function may be determined from a contribution of each event by taking the reciprocal of the volume in which each event could have been observed (i.e. $1/V_{\max,i}$), and binning in terms of energy.

In the case of an evolving population (e.g. source density evolving with redshift, or source luminosity variations; Schmidt 1968; Macquart & Ekers 2018b) or incorrect assumptions regarding the nature of the volume, the distribution given through equation (1) will not, in general, be uniform. Re-weighting V by the correct source density, ψ, within that volume, that is, $V \to V' = V \cdot \psi\,(V)$, would, however, restore the distribution to uniformity.

Measurement of the FRB luminosity distribution presents a number of complications not typically encountered with static sources, since it is not possible to find all objects by scanning an area of sky with uniform sensitivity. For a sample of static sources, one may clearly define the volume over which a source would have been detectable, viz., the volume of a spherical sector whose radius is governed by the luminosity distance out to which an object could have been detected, given the telescope sensitivity. For radio transients such as FRBs, however, this is not the case: the instantaneous sensitivity across the FoV, when the FRB is detected, is non-uniform and the volume probed is therefore not a section of a sphere. When one is interested in the event rate rather than the source density per comoving volume, the additional effect of the observing time and time dilation as a function of distance needs to be taken into account.

The spectral energy density, $E_{\nu,0}$, of a given FRB, its observed fluence, $F_{\nu,0}$, and its luminosity distance, D_L, are related via equation (2)

$$E_{\nu,0} = \frac{4\pi F_{\nu,0} D_L^2}{(1+z_b)^{2+\alpha}}, \tag{2}$$

where z_b is the redshift of the FRB and α the fluence spectral index. We define α:$F_\nu \propto \nu^\alpha$ – this is now common usage, however it is the opposite sign convention to that used in Macquart & Ekers (2018b) and subsequently in Arcus et al. (2020) and (2022).

2.2 The survey volume

Here we derive measures of both V and $V_{\max}$ that account for the beamshape of the FRB discoveryp antenna. We note that, for a non-evolving population in a Cartesian Universe, the antenna beamshape will not affect calculations of $V/V_{\max}$, since both V and $V_{\max}$ will scale identically for all beam positions. Assuming a constant value of beam (hence telescope) sensitivity will, however, smear-out the luminosity function due to uncorrected-for differences between true fluence (which requires the beamshape at point of detection to be known) and the fluence calculated when ignoring beamshape.

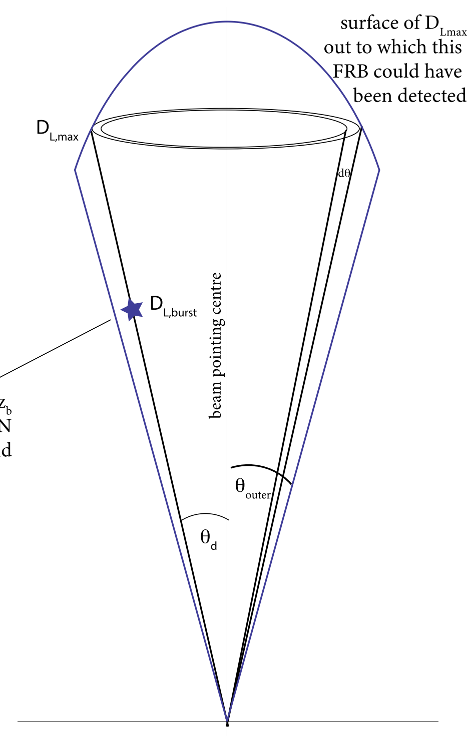

Figure 1. The geometry of the $V_{\max}$ region defining the total comoving volume out to which a given FRB may be detected with an S/N being a factor of X above the threshold detection S/N for a generic beam. Note that $V_{\max}$ must be computed separately for each FRB since the S/N of a given FRB depends upon both the FRB fluence and duration: the $D_{L,\max}$ surface cannot be specified solely in terms of a threshold fluence.

In the case of an evolving population, objects requiring spectral corrections, and/or a non-Euclidean Universe, the proportionality between V and $V_{\max}$ is lost, and beamshape corrections can become important in calculating $V/V_{\max}$ as well as the luminosity function. Given that the FRB population may experience both source evolution and spectral dependence, and FRB observations now probe the $z > 1$ regime at which cosmological distance measures are significantly different from their Euclidean equivalents, we consider a proper treatment crucial when applying the $V/V_{\max}$ method.

2.2.1 The maximum volume probed by a generic beam

Consider a FRB event occurring at a given offset, θ_d, from the beam centre of a generic telescope beam at an S/N value that is a factor of X above the cut-off S/N flux threshold S_{cutoff} (see Fig. 1). We would like to know over what volume this particular event, with FRB spectral energy density, E_ν, and burst-width, Δt, could have been detected. If the telescope beam is circularly symmetric,

https://doi.org/10.1017/pasa.2024.114 Published online by Cambridge University Press

the comoving volume of space probed out to a redshift $z_{\max}$ is given by

$$V_{\max} = \int\int \frac{D_H}{E(z)} \frac{D_L^2(z)}{(1+z)^2} dz d\Omega \\ = 2\pi \int_0^{\theta_{\text{outer}}} \int_0^{z_{\max}(\theta)} \frac{D_H}{E(z)} \frac{D_L^2(z)}{(1+z)^2} \sin\theta \, d\theta dz, \quad (3)$$

where Ω is the solid angle of the telescope beam on the sky; θ, the bore-sight angle of the telescope beam; and θ_{outer} the outermost detectable angle of the beam. Moreover, $z_{\max}(\theta)$ is the redshift of the maximum luminosity distance that an event could be detected in the telescope beam and D_H and $D_L(z)$ are the Hubble distance and luminosity distance for a given redshift, z, respectively.

We write $z_{\max}(\theta)$ as an explicit function of θ to emphasise that the telescope probes to a larger redshift at the beam centre relative to its periphery. We take the integral over the angular distance to extend out to an effective beam cut-off point; the objective here being to find $z_{\max}(\theta)$ for a given FRB so that the effective survey volume may be determined.

We may compute the maximum detectable luminosity distance for each FRB at its particular location within the telescope beam via equation (2), to determine $E_{\nu,0}$, then find the luminosity distance at which the FRB of this energy density would be detectable at the threshold S_{cutoff}.

An additional complication is that the detection S/N is not determined just by the FRB flux density; rather, S/N is proportional to a product involving the FRB flux density and its duration. Thus the threshold fluence is obtained by solving

$$\frac{S_{\text{cutoff}}}{S} \equiv X(\theta_d) = \frac{S_{\nu,0}\,\Delta t_0^{1/2}}{S_{\nu,\text{cutoff}}\,\Delta t_{\text{cutoff}}^{1/2}} \\ = \frac{F_{\nu,0}}{F_{\nu,\text{cutoff}}} \frac{(1+z)^{-1/2}}{(1+z_{\max})^{-1/2}}. \quad (4)$$

The solution of equation (4) yields the following transcendental equation for the limiting detectable fluence for a given FRB:

$$F_{\nu,\text{cutoff}} = \frac{F_{\nu,0}}{X(\theta_d)} \left(\frac{1+z_b}{1+z_{\max}}\right)^{-1/2}, \quad (5)$$

and we solve this equation to determine $z_{\max}(\theta)$.

Yet a further complication is that the telescope detection efficiency decreases with increasing DM, which is nearly linearly proportional to redshift at $z \lesssim 1$ (see e.g. Arcus et al. 2022). If the telescope efficiency, η, is written in terms of DM, the maximum luminosity distance out to which the FRB is detectable[a] is given by:

$$D_{L,\text{cutoff}} = D_{L,b}\, X^{1/2}(\theta_d) \left(\frac{1+z_{\max}}{1+z_b}\right)^{(3/2+\alpha)/2} \\ \left(\frac{\eta(\text{DM}(z_{\max}))}{\eta(\text{DM}(z_b))}\right)^{1/2}, \quad (6)$$

where we note explicitly that $\text{DM} = \text{DM}(z)$.

$z_{\max}(\theta)$ may therefore be determined by noting that $X(\theta)$ changes according to the position in the beam. For a telescope beam whose sensitivity falls off as $B(\theta)$, telescope sensitivity changes as

$$X(\theta) = X(\theta_d) \frac{B(\theta)}{B(\theta_d)}. \quad (7)$$

Thus the limiting redshift at an angular distance, θ, from the beam centre may be found by solving the following equation for $z_{\max}(\theta)$ via

$$D_{L,\max} = D_{L,b} X^{1/2}(\theta_d) \left(\frac{1+z_{\max}}{1+z_b}\right)^{(3/2+\alpha)/2} \\ \left(\frac{B(\theta)}{B(\theta_d)} \frac{\eta(\text{DM}(z_{\max}))}{\eta(\text{DM}(z_b))}\right)^{1/2}. \quad (8)$$

Determination of $z_{\max}(\theta)$ via equation (8) is fully prescribed in terms of: (i) the FRB detection angle from beam centre, θ_d; (ii) the factor above the cut-off S/N threshold, $X(\theta_d)$; (iii) the FRB redshift, z_b; (iv) the beam pattern, $B(\theta)$; and (v) the telescope efficiency, $\eta(\text{DM};w)$. The maximum volume in which the FRB could have been detected, $V_{\max}$, may then be determined using equation (3).

2.2.2 The detection volume of a FRB within a generic beam

The volume in which a FRB is detected, V, for a generic beam may be determined via

$$V = 2\pi \left(\int_0^{\theta_{\max}} \int_0^{z_b} \frac{D_H}{E(z)} \frac{D_L^2(z)}{(1+z)^2} \sin\theta \, d\theta dz \right. \\ \left. + \int_{\theta_{\max}}^{\theta_{\text{outer}}} \int_0^{z_{\max}(\theta)} \frac{D_H}{E(z)} \frac{D_L^2(z)}{(1+z)^2} \sin\theta \, d\theta dz \right), \quad (9)$$

where we integrate the constant luminosity distance of the detected FRB out to maximum angle, $\theta_{\max}$, at the detection threshold (i.e. at the beam cut-off fluence, see equation (10)), then add the residual volume out to the limit of integration, θ_{outer}. For an overview of determining $V/V_{\max}$ in relation to a non-uniform sensitivity, see Appendix B.

By rearranging and relabelling equation (8), and making the substitution $X(\theta_{\max})B(\theta_{\max}) \to B^2(\theta_{\max})X(\theta_{\text{d}})/B(\theta_{\text{d}})$ via equation (7), $\theta_{\max}$ may be determined by solving

$$B^2(\theta_d)\, D_L^2(z_b)\, \eta(\text{DM}(z_b))\, (1+z_{\max})^{2+\alpha} = \\ B^2(\theta_{\max})\, D_L^2(z_{\max})\, \eta(\text{DM}(z_{\max}))\, (1+z_b)^{2+\alpha}. \quad (10)$$

2.3 The volume probed by a specific beam

We further adapt the treatment of Section 2.2 to admit telescopes with arbitrary beamshapes (later in Section 3 we specifically admit the ASKAP telescope beamshape).

For a beam viewing a solid angle of sky, the inverse beamshape, $\Omega(B)$ (James et al. 2021a) with beam function $B(\theta)$, the maximum volume in which a FRB may have been detected, may be recast as

$$V_{\max} = \int\int \frac{D_H}{E(z)} \frac{D_L^2(z)}{(1+z)^2} dz d\Omega \\ = \int_0^1 \int_0^{z_{\max}(B)} \frac{D_H}{E(z)} \frac{D_L^2(z)}{(1+z)^2} \Omega(B)\, dz\, dB. \quad (11)$$

[a] We may see this by directly placing η for the flux density terms in equation (4).

https://doi.org/10.1017/pasa.2024.114 Published online by Cambridge University Press

Likewise the volume in which the FRB was detected, for a specific beam-shape, is recast as

$$V = \int_0^{B_0(\theta_d)} \int_0^{z_{\max}(B)} \frac{D_H}{E(z)} \frac{D_L^2(z)}{(1+z)^2}\, \Omega(B)\, dz\, dB + \int_{B_0(\theta_d)}^1 \int_0^{z_b} \frac{D_H}{E(z)} \frac{D_L^2(z)}{(1+z)^2}\, \Omega(B)\, dz\, dB, \quad (12)$$

where $B_0(\theta_d) = B(\theta_d)/X(\theta_d)$.

In order to determine the limits of integration in equation (12) and to solve equation (8) for $z_{\max}(B)$, we utilise an Airy beam function as the underlying beam model where necessary (Arcus et al. 2022).

Furthermore, consistent with (James et al. 2021a, see Section 4.3 Numerical implementation), equations (11) & (12) are implemented as histogram approximations (i.e. Riemann sums), such that $\int B(\Omega)\, dB \approx \sum_{i=1}^{N_B} \Omega(B)\Delta B$ where we choose $N_B = 10$ (James et al. 2021a).

As the source evolution function for FRBs is hitherto unknown, considered hypotheses generally take on the form of some function of the star formation rate (SFR; e.g. Macquart & Ekers 2018b), or delayed with respect to star formation (e.g. Cao, Yu, & Zhou 2018). Current fitting methods favour source evolution consistent with the cosmic star formation rate (James et al. 2022; Shin et al. 2023), although this is equally consistent with a generic $(1 + z)^n$ model. We show in Appendix A that with current data, the $V/V_{\max}$ method cannot currently discriminate between source evolution models. Accordingly, we choose the simpler case of no source evolution and set $V' = V$ as discussed in Appendix A.

3. Application to ASKAP

We consider two discrete samples from the ASKAP telescope: the full set of 63 FRBs and a subset of 28 FRBs for which an identified host galaxy with measured redshift z has been obtained. We treat these two samples separately in order to determine whether the use of FRBs from the DM-only inferred redshift sample yields an energy distribution consistent with those from which redshift has been independently determined. We examine the FRB population and apply the luminosity-volume- or $V/V_{\max}$-test to examine the source distribution of these transient sources, accounting for cosmological and instrumental effects, in order to determine the RLF for the sampled population. In Appendix A, we consider both $\alpha = 0$ and $\alpha = -1.5$ (Macquart et al. 2019), and also a cosmological evolution of the source population. However, we find little discriminating power between the two, hence we choose, hereinafter, $\alpha = 0$ and no source evolution for simplicity.

We use the formalism outlined in Section 2.3 to determine the volumetrics necessary to conduct the $V/V_{\max}$-test and apply the beamshape for the ASKAP telescope, as given by James et al. (2021a, see Figure 3 of Section 4.1 therein), via the inverse beamshape, $\Omega(B)$. We choose this approach to represent a realistic beamshape for ASKAP and to avoid complications in cases where a FRB detection occurs either in multiple beams or in an outer beam. Due to ASKAP's beams overlapping approximately at the half-power points, the effect of beamshape in this analysis is not strong, and a short investigation shows that the effect of ignoring it for both and the luminosity function is minor.

Table 1 lists the candidate localised sample of FRBs along with their relevant observational parameters applicable to our analysis. Since there is some suggestion that ASKAP ICS observations are incomplete in the range S/N < 14 (Shannon et al. 2024), and we wish to ensure the localised sample has minimum bias, only those FRBs for which the S/N exceeds the threshold of $\mathrm{S/N_{cutoff}} = 14$ were subsequently admitted for further analysis. These are listed in Table 2 and are hereinafter identified as the Localised High S/N Sample, comprising 19 FRBs.

Table 3 lists the candidate full sample comprising 63 ASKAP FRBs along with their relevant observational parameters applicable to our analysis. In this sample, we include the 28 FRBs localised to their host galaxies. This constitutes the Full Sample (see Table 3), where the detection threshold of $\mathrm{S/N_{cutoff}} = 9.5$ as used in the CRAFT detection pipeline, is used for all FRBs irrespective of considerations of potential bias. The derived parameters of the Full Sample are provided in Table 4, whereby redshifts, even for FRBs with measured redshift, have been estimated from their DM budget via

$$\mathrm{DM_{Obs}} = \mathrm{DM_{MW}} + \mathrm{DM_{Halo}} + \mathrm{DM_{cosmic}} + \mathrm{DM_{Host}}/(1+z), \quad (13)$$

where $\mathrm{DM_{Obs}}$ is the observed DM of the FRB, while DM_MW, $\mathrm{DM_{Halo}}$ and $\mathrm{DM_{Host}}$ are the DM contributions due to the Milky Way disc, its halo, and the FRB host environment, respectively. We set the cosmological contribution $\mathrm{DM_{cosmic}}$ to its mean, $\overline{\mathrm{DM}}(z)$, using equation (14) and assume a constant host contribution of $\mathrm{DM_{Host}} = 50$ pc cm^{-3} and halo contribution of $\mathrm{DM_{Halo}} = 50$ pc cm^{-3} consistent with Arcus et al. (2020). $\mathrm{DM_{MW}}$ is determined via the NE2001 model of Cordes & Lazio (2003). We note that uncertainties in these quantities can be large – of order a factor of two for $\mathrm{DM_{MW}}$ (Schnitzeler 2012), and perhaps a similar uncertainty for $\mathrm{DM_{Halo}}$ (Prochaska & Zheng 2019; Keating & Pen 2020). Fluctuations in $\mathrm{DM_{Host}}$ are not directly measured, but are estimated to be large (James et al. 2022). This results in potentially large fluctuations about the Macquart relation, as evinced by FRBs with exceptionally low or high DMs for their redshifts, for example, FRB 20200120E with DM 87.82 pc cm^{-3} at 3.6 Mpc (Bhardwaj et al. 2021), and FRB 20190520B with DM 1204.7 pc cm^{-3} at $z = 0.241$ (Niu et al. 2022a).

Consistent with Macquart et al. (2020) and Arcus et al. (2022), we determine the mean DM of a homogeneously distributed intergalactic medium (IGM) as given by Ioka (2003), Inoue (2004), updated to include the fraction f_d of baryons in diffuse ionised gas as per Deng & Zhang (2014)

$$\overline{\mathrm{DM}}(z) = \frac{3H_0 c\Omega_b}{8\pi G m_p} \int_0^z f_d(z') \frac{(1+z')\left[\frac{3}{4}X_{\mathrm{e,H}}(z') + \frac{1}{8}X_{\mathrm{e,He}}(z')\right]}{\sqrt{(1+z')^3\Omega_m + \Omega_\Lambda}}\, dz', \quad (14)$$

where the ionised fractions of Hydrogen and Helium are taken to be $X_{\mathrm{e,H}} = 1$ for $z < 8$ and $X_{\mathrm{e,He}} = 1$ for $z < 2.5$, respectively, or zero otherwise. Throughout this work we adopt a ΛCDM universe with the cosmological parameters $(h, H_0, \Omega_b, \Omega_m, \Omega_\Lambda, \Omega_k) = (0.7, 100h\mathrm{kms^{-1}Mpc^{-1}}, 0.0486, 0.308, 0.691, 0)$, that is, an intermediate value of H_0 (Abdalla et al. 2022), but otherwise in accordance with the (Planck Collaboration et al. 2016). We use the estimate of $f_d(z)$ from the FRB code base (Prochaska et al. 2019a), which ranges from 0.844 at $z = 0$, and increases slowly with redshift. This relation between FRB redshift and expected DM was first verified by Macquart et al. (2020), and is now known as the Macquart relation. Fig. 2 illustrates the scatter about the Macquart

https://doi.org/10.1017/pasa.2024.114 Published online by Cambridge University Press

Table 1. Properties of the 28 localised ASKAP candidate FRBs for which a host galaxy redshift has been determined. FRBs identified with an asterisk below ($*$) are excluded from subsequent analysis since their detected S/N < S/N_{cutoff} ($=14$). Variables listed in this table are: (i) DM – Observed DM; (ii) ν_c – Centre Frequency; (iii) S/N – Primary S/N; (iv) $S/N_{cuttoff}$ – S/N threshold; (v) DM_{Gal} – DM of Milky Way disc using the NE2001 model; (vi) Δt – Sample Interval; (vii) w – Fitted Pulse-width (FWHM); (viii) θ_d – Detection Angle; (ix) F_ν – Corrected Fluence; & (x) z_{loc} – Localized host redshift. References are: a: Bannister et al. (2017), b: Shannon et al. (2018), c: Mahony et al. (2018), d: Macquart et al. (2019), e: Agarwal et al. (2019), f: Qiu et al. (2019), g: Bhandari et al. (2019), h: Bannister et al. (2019), i: Prochaska et al. (2019b), j: Macquart et al. (2020), k: Heintz et al. (2020), l: Bhandari et al. (2020), m: Bhandari et al. (2022), n: Bhandari et al. (2023) o: (Shannon et al. 2024), p: James et al. (2022), q: Baptista et al. (2024), r: Ryder et al. (2023), s: Gordon et al. (2024).

Name	S/N	DM ($pc\,cm^{-3}$)	DM_{Gal} ($pc\,cm^{-3}$)	ν_c (MHz)	Δt (ms)	w (ms)	θ_d (°)	F_ν (Jy ms)	z_{loc}	Reference
FRB 20171020A	19.5	114.1	38.4	1 297.5	1.260	1.70	0.722	200	0.00867	c
FRB 20180924B	21.1	362.4	40.5	1 297.5	0.864	1.76	0.23	18	0.3214	h
FRB 20181112A	19.3	589.0	40.2	1 297.5	0.864	2.10	0.31	28	0.4755	i
FRB 20190102C	14.0	364.5	57.3	1 271.5	0.864	1.70	0.23	16	0.29	j
FRB 20190608B	16.1	339.5	37.2	1 271.5	1.728	6.00	0.36	28	0.1178	j
FRB 20190611B($*$)	9.5	322.2	57.6	1 271.5	1.728	2.00	0.48	10	0.378	j
FRB 20190711A	23.8	594.6	56.6	1 271.5	1.728	6.50	0.08	36	0.522	j
FRB 20190714A($*$)	10.7	504.7	38.5	1 271.5	1.728	2.90	0.46	12	0.2365	k
FRB 20191001A	37.1	506.9	44.2	919.5	1.728	4.20	0.58	120	0.23	l
FRB 20191228A	22.9	297.5	32.9	1 271.5	1.728	2.30	0.49	67	0.240	m
FRB 20200430A($*$)	13.9	380.1	27.0	864.5	1.728	6.50	0.48	35	0.161	k
FRB 20200906A($*$)	10.5	577.8	35.9	864.5	1.728	6.00	0.65	53	0.36879	m
FRB 20210117A	27.1	730.0	34.4	1 271.5	1.182	3.2	0.464	36	0.214	n
FRB 20210320C	15.3	384.0	42	864.5	1.182	5.4	1.12	59	0.28	o
FRB 20210807D	47.1	251.9	121.2	920.5	1.182	10.00	0.453	100	0.12969	p
FRB 20211127I	37.9	234.8	42.5	1 271.5	1.182	1.41	0.16	35	0.046946	p
FRB 20211203C	14.2	636.2	63.4	920.5	1.182	9.60	0.212	30	0.34386	o,q
FRB 20211212A($*$)	12.8	206.0	27.1	1 632.5	1.182	2.70	0.77	131	0.0715	p
FRB 20220105A($*$)	9.8	583.0	22.0	1 632.5	1.182	2.00	0.443	19	0.2785	o,q
FRB 20220501C	16.1	449.5	30.6	863.5	1.182	6.50	0.516	32	0.381	o,q
FRB 20220610A	29.8	1458.1	31.0	1 271.5	1.182	5.60	0.073	47	1.016	r,s
FRB 20220725A($*$)	12.7	290.4	30.7	920.5	1.182	4.10	1.272	72	0.1926	o
FRB 20220918A	26.4	657	41	1 271.5	1.182	7.1	0.457	55	0.491	o,q
FRB 20230526A	22.1	361.4	50	1 271.5	1.182	4.7	0.383	34	0.157	o
FRB 20230708A	31.5	411.5	50.2	920.5	1.182	23.6	0.657	111	0.105	o
FRB 20230718A($*$)	10.9	477	395.6	1 271.5	1.182	3.5	0.317	14	0.035	o
FRB 20230902A($*$)	11.8	440	34.3	831.5	1.182	5.9	0.63	23	0.3619	o
FRB 20231226A	36.7	329.9	38	863.5	1.182	11.8	0.739	78	0.1569	o

relation for the Localised High S/N Sample of FRBs. The scatter is large – up to a factor of two in redshift – and dominates over the uncertainties in the mean of the Macquart relation. We therefore estimate the error from using the Full Sample by comparing it to that of the Localised High S/N Sample, rather than marginalising over uncertainties in estimating z_{DM}. Three FRBs have an implied negative z_{DM}, and hence are omitted from our initial analysis of the Full Sample. The effects of this are discussed in Section 4.2.

4. Discussion

4.1 The FRB radio luminosity function

The distributions of V/V_{max} for both samples are shown in Fig. 3. As discussed in Appendix A, the major deviation from uniformity is the deficit of FRBs with low V/V_{max}, which cannot be rectified for any reasonable source evolution function. Hence, we proceed to calculate the RLF from these samples, under the assumption of no spectral dependence (i.e. $\alpha = 0$) and no cosmological evolution of the source population.

Fig. 4 depicts the derived RLF from the Localised High S/N Sample and Full Sample. Also shown are their best-fit functions (fitted parameters given in Table 5) and comparisons to values from the literature. A flatter RLF is preferred by the Full Sample ($\gamma = -1.82 \pm 0.12$) compared to the Localised High S/N Sample ($\gamma = -2.11 \pm 0.18$). At high luminosities, the Full Sample shows some evidence for a high-energy downturn near $\log_{10} E_{max}\,(\mathrm{J\,Hz^{-1}}) = 25.8 \pm 0.39$ — likely due to the smaller Localised High S/N Sample containing no data in the 10^{26}–10^{27} J Hz^{-1} bin. Conversely, the RLF data at $E_\nu < 10^{23}$ J Hz^{-1} from the Localised High S/N Sample shows an excess which is inconsistent with both a power-law or Schechter function, and the

Table 2. Derived properties of the 19 *Localised High S/N Sample* of ASKAP FRBs for which the S/N exceeds the threshold $\mathrm{S/N} \geq \mathrm{S/N}_{\mathrm{cutoff}}(=14)$, for fluence spectral indices of $\alpha = 0.0$, and no source evolution. Note that this sample is a subset of the FRBs listed in Table 1.

Name	D_L (Gpc)	E_ν (J Hz^{-1})	z_{max}	$D_{L,\mathrm{max}}$ (Gpc)	V_{max} (Gpc^3)	V/V_{max}
FRB 20171020A	0.037	3.30×10^{22}	0.017	1.93×10^{2}	6.66×10^{2}	0.290
FRB 20180924A	1.68	3.56×10^{24}	0.410	5.09×10^{6}	6.38×10^{6}	0.797
FRB 20181112B	2.66	1.09×10^{25}	0.605	1.36×10^{7}	1.66×10^{7}	0.821
FRB 20190102A	1.49	2.56×10^{24}	0.303	2.92×10^{6}	2.94×10^{6}	0.995
FRB 20190608C	0.549	8.07×10^{23}	0.143	3.0×10^{5}	3.51×10^{5}	0.854
FRB 20190711A	2.98	1.65×10^{25}	0.730	1.64×10^{7}	2.22×10^{7}	0.742
FRB 20191001A	1.15	1.25×10^{25}	0.429	2.67×10^{6}	7.14×10^{6}	0.374
FRB 20191228A	1.22	7.71×10^{24}	0.389	2.78×10^{6}	5.39×10^{6}	0.516
FRB 20210117A	1.06	3.26×10^{24}	0.362	2.06×10^{6}	4.52×10^{6}	0.455
FRB 20210320A	1.43	8.84×10^{24}	0.477	4.36×10^{6}	9.47×10^{6}	0.460
FRB 20210807D	0.609	3.47×10^{24}	0.275	5.57×10^{5}	2.10×10^{6}	0.265
FRB 20211127I	0.208	1.66×10^{23}	0.079	2.71×10^{4}	6.49×10^{4}	0.418
FRB 20211203C	1.82	6.56×10^{24}	0.354	4.13×10^{6}	4.14×10^{6}	0.998
FRB 20220501C	2.05	8.41×10^{24}	0.452	7.35×10^{6}	8.20×10^{6}	0.897
FRB 20220610A	6.70	6.22×10^{25}	1.590	7.59×10^{7}	1.07×10^{8}	0.710
FRB 20220918A	2.76	2.26×10^{25}	0.927	1.67×10^{7}	3.67×10^{7}	0.455
FRB 20230526A	0.749	1.71×10^{24}	0.231	7.84×10^{5}	1.31×10^{6}	0.598
FRB 20230708A	0.485	2.56×10^{24}	0.201	2.92×10^{5}	8.95×10^{5}	0.326
FRB 20231226A	0.749	3.91×10^{24}	0.336	9.52×10^{5}	3.56×10^{6}	0.267

Table 3. Properties of the *Full Sample*. Columns and references are the same as in Table 1, excepting z_{DM} – Redshift inferred from the $z-\mathrm{DM}$ relation.

Name	DM (pc cm^{-3})	ν_c (MHz)	S/N	$\mathrm{DM}_{\mathrm{Gal}}$	Δt (pc cm^{-3})	w (ms)	θ_d (ms)	F_ν (°)	z_{DM} (Jy ms)	Reference
FRB 20170107A	610	1 320.5	16	37	1.26	2.4	0.163	58	0.506	a
FRB 20170416A	523	1 320.5	13.1	40	1.26	5	0.332	96	0.413	b
FRB 20170428A	992	1 320.5	10.5	40	1.26	4.4	0.041	34	0.891	b
FRB 20170712A	313	1 296.5	12.7	39	1.26	3.5	0.281	52	0.193	b
FRB 20170707A	235	1 296.5	9.5	36	1.26	1.4	0.133	54	0.111	b
FRB 20170906A	390	1 296.5	17	39	1.26	2.5	0.237	74	0.275	b
FRB 20171003A	463	1 297.5	13.8	41	1.26	2	0.342	82	0.350	b
FRB 20171004A	304	1 297.5	10.9	39	1.26	2	0.203	44	0.184	b
FRB 20171019A	461	1 297.5	23.4	37	1.26	5.4	0.379	219	0.352	b
FRB 20171020A*	114	1 297.5	19.5	38	1.26	1.7	0.630	200	-0.02	b,c
FRB 20171116A	619	1 297.5	11.8	36	1.26	3.2	0.346	64	0.516	b
FRB 20171213A	159	1 297.5	25.1	37	1.26	1.5	0.513	133	0.024	b
FRB 20171216A#	203	1297.5	8	37	1.26	1.9	0.491	40	0.074	b
FRB 20180110A	716	1 297.5	35.6	39	1.26	7.88	0.430	422	0.612	b
FRB 20180119A	403	1 297.5	15.9	36	1.26	2.7	0.298	110	0.292	b
FRB 20180128A	441	1 297.5	12.4	32	1.26	2.9	0.158	51	0.336	b
FRB 20180128B	496	1 297.5	9.6	41	1.26	2.3	0.396	66	0.384	b
FRB 20180130A	344	1 297.5	10.3	39	1.26	4.1	0.380	95	0.227	b
FRB 20180131A	658	1 297.5	13.8	40	1.26	4.5	0.391	100	0.552	b
FRB 20180212A	168	1 297.5	18.3	31	1.26	1.81	0.391	96	0.041	b

https://doi.org/10.1017/pasa.2024.114 Published online by Cambridge University Press

Table 3. (Continued)

Name	DM (pc cm^{-3})	ν_c (MHz)	S/N	DM$_{\rm Gal}$	Δt (pc cm^{-3})	w (ms)	θ_d (ms)	F_ν (°)	$z_{\rm DM}$ (Jy ms)	Reference
FRB 20180315A	479	1 297.5	10.5	101	1.26	2.4	0.395	56	0.304	d
FRB 20180324A	431	1 297.5	9.8	64	1.26	4.3	0.494	71	0.292	d
FRB 20180417A	475	1 297.5	17.5	26	1.26	2.3	0.458	49	0.378	e
FRB 20180430A*	264	1 297.5	28.2	169	1.26	1.2	0.392	177	-0.00	f
FRB 20180515A	355	1 297.5	12.1	33	1.26	1.9	0.191	46	0.245	g
FRB 20180525A	388	1 297.5	27.4	31	1.26	3.8	0.510	300	0.282	d
FRB 20180924B	362	1 297.5	21.1	41	0.864	1.76	0.234	18	0.244	h
FRB 20181112A	589	1 297.5	19.3	40	0.864	2.1	0.312	28	0.481	i
FRB 20190102C	365	1 271.5	14	57	0.864	1.7	0.229	16	0.230	j
FRB 20190608B	340	1 271.5	16.1	37	1.728	6	0.362	28	0.224	j
FRB 20190611B	322	1 271.5	9.5	58	1.728	2	0.481	10	0.182	j
FRB 20190711A	595	1 271.5	23.8	57	1.728	6.5	0.079	36	0.470	j
FRB 20190714A	505	1 271.5	10.7	39	1.728	2.9	0.458	13	0.396	k
FRB 20191001A	507	919.5	37.1	44	1.728	4.2	0.579	120	0.393	l
FRB 20191228A	298	1 271.5	22.9	33	1.728	2.3	0.486	67	0.184	m
FRB 20200430A	380	864.5	13.85	27	1.728	6.5	0.475	35	0.278	k
FRB 20200627A	294	920.5	11.0	40	1.728	11	0.340	28	0.172	o
FRB 20200906A	578	864.5	10.5	36	1.728	6	0.570	53	0.474	m
FRB 20210117A	730	1 271.5	27.1	34	1.182	3.2	0.464	36	0.631	n
FRB 20210214G	398	1 271.5	11.6	32	1.182	3.5	0.442	13	0.291	o
FRB 20210320C	384	864.5	15.3	42	1.182	5.4	1.146	59	0.266	o
FRB 20210407E	1785	1 271.5	19.1	154	1.182	6.6	0.370	36	1.581	o
FRB 20210807D	252	920.5	47.1	121	1.182	10	0.602	100	0.034	p
FRB 20210809C	652	920.5	16.8	190	1.182	14	0.190	45	0.392	o,p
FRB 20210912A	1235	1 271.5	31.7	31	1.182	5.5	0.475	70	1.146	o,p
FRB 20211127I	235	1 271.5	37.9	43	1.182	1.4	0.161	35	0.103	p
FRB 20211203C	636	920.5	14.2	63	1.182	9.6	0.212	30	0.506	o,q
FRB 20211212A	206	1 632.5	12.8	27	1.182	2.7	0.772	131	0.089	p
FRB 20220105A	583	1 632.5	9.8	22	1.182	2.0	0.443	19	0.494	o,q
FRB 20220501C	450	863.5	16.1	31	1.182	6.5	0.516	32	0.347	o,q
FRB 20220531A	727	1 271.5	9.7	70	1.182	11.0	0.790	30	0.592	o,q
FRB 20220610A	1458	1 271.5	29.8	31	1.182	5.6	0.073	47	1.373	r,s
FRB 20220725A	290	920.5	12.7	31	1.182	4.1	1.272	72	0.177	o,q
FRB 20220918A	657	1 271.5	26.4	41	1.182	7.1	0.457	55	0.550	o,q
FRB 20221106A	344	1 631.5	35.1	35	1.182	5.7	0.361	80	0.231	o,q
FRB 20230521A	640.2	831.5	15.2	42	1.182	16.5	0.401	34	0.532	o
FRB 20230526A	361.4	1 271.5	22.1	50	1.182	4.7	0.383	34	0.233	o
FRB 20230708A	411.5	920.5	31.5	50	1.182	23.6	0.657	111	0.286	o
FRB 20230718A*	477	1 271.5	10.9	396	1.182	3.5	0.317	14	-0.02	o
FRB 20230731A	701	1 271.5	16.6	547	1.182	3.5	0.510	25	0.061	o
FRB 20230902A	440	831.5	11.8	34	1.182	5.9	0.630	23	0.333	o
FRB 20231006A	509.7	863.5	15.2	68	1.182	8.3	0.534	25	0.371	o
FRB 20231226A	329.9	863.5	36.7	38	1.182	11.8	0.739	78	0.213	o

*These FRBs have $z_{\rm DM} < 0$, and are excluded from initial analysis.
#This FRB has S/N$_{\rm cutoff} = 8$; all others are 9.5.
*These FRBs have $z_{\rm DM} < 0$, and are excluded from initial analysis.

https://doi.org/10.1017/pasa.2024.114 Published online by Cambridge University Press

Table 4. Derived properties of the *Full Sample* for a fluence spectral index of $\alpha = 0.0$ and no source evolution. For those with $z_{\mathrm{DM}} < 0$ (marked with a *: FRB 20171020A, FRB 20180430A, and FRB 20230718A), an assumed distance of 2 Mpc is used. Columns are identical to those of Table 2.

Name	D_L (Gpc)	E_ν (J Hz^{-1})	$z_{\max}$ (Gpc)	$D_{L,\max}$ (Gpc^3)	$V_{\max}$	V/$V_{\max}$
FRB 20170107A	2.988	2.67×10^{25}	0.696	1.75×10^{7}	2.25×10^{7}	0.778
FRB 20170416A	2.357	3.12×10^{25}	0.590	1.03×10^{7}	1.39×10^{7}	0.743
FRB 20170428A	5.895	3.85×10^{25}	0.970	4.25×10^{7}	$4.27 \cdot 10^{7}$	0.995
FRB 20170712A	0.995	4.26×10^{24}	0.256	1.41×10^{6}	$1.74 \cdot 10^{6}$	0.810
FRB 20170707A	0.547	1.55×10^{24}	0.119	2.15×10^{5}	2.15×10^{5}	1.000
FRB 20170906A	1.478	1.17×10^{25}	0.410	4.02×10^{6}	6.13×10^{6}	0.657
FRB 20171003A	1.943	1.99×10^{25}	0.486	7.26×10^{6}	9.71×10^{6}	0.747
FRB 20171004A	0.940	3.27×10^{24}	0.215	1.06×10^{6}	1.11×10^{6}	0.959
FRB 20171019A	1.957	5.37×10^{25}	0.736	8.56×10^{6}	2.29×10^{7}	0.374
FRB 20171116A	3.060	3.05×10^{25}	0.675	1.70×10^{7}	2.02×10^{7}	0.844
FRB 20171213A	0.114	1.96×10^{23}	0.054	5.29×10^{3}	2.17×10^{4}	0.244
FRB 20171216A	0.358	5.27×10^{23}	0.099	9.96×10^{4}	1.25×10^{5}	0.797
FRB 20180110A	3.748	2.66×10^{26}	1.996	3.48×10^{7}	1.38×10^{8}	0.252
FRB 20180119A	1.581	1.93×10^{25}	0.436	4.67×10^{6}	7.10×10^{6}	0.658
FRB 20180128B	1.857	1.15×10^{25}	0.413	5.60×10^{6}	6.16×10^{6}	0.910
FRB 20180128A	2.165	1.89×10^{25}	0.464	7.97×10^{6}	8.61×10^{6}	0.926
FRB 20180130A	1.187	1.05×10^{25}	0.288	2.05×10^{6}	2.35×10^{6}	0.873
FRB 20180131A	3.313	5.32×10^{25}	0.841	2.13×10^{7}	3.12×10^{7}	0.684
FRB 20180212A	0.196	4.05×10^{23}	0.071	2.21×10^{4}	4.78×10^{4}	0.462
FRB 20180315A	1.653	1.06×10^{25}	0.386	4.62×10^{6}	5.34×10^{6}	0.866
FRB 20180324A	1.581	1.25×10^{25}	0.401	4.29×10^{6}	5.54×10^{6}	0.774
FRB 20180417A	2.125	1.36×10^{25}	0.647	9.98×10^{6}	1.90×10^{7}	0.524
FRB 20180515A	1.294	5.84×10^{24}	0.298	2.51×10^{6}	2.74×10^{6}	0.915
FRB 20180525A	1.517	4.93×10^{25}	0.699	5.36×10^{6}	2.12×10^{7}	0.253
FRB 20180924B	1.287	2.32×10^{24}	0.394	3.16×10^{6}	5.75×10^{6}	0.551
FRB 20181112A	2.817	1.18×10^{25}	0.770	1.74×10^{7}	2.85×10^{7}	0.611
FRB 20190102C	1.205	1.81×10^{24}	0.302	2.35×10^{6}	2.91×10^{6}	0.809
FRB 20190608B	1.174	3.03×10^{24}	0.361	2.39×10^{6}	4.20×10^{6}	0.570
FRB 20190611B	0.934	7.35×10^{23}	0.236	1.21×10^{6}	1.45×10^{6}	0.838
FRB 20190711A	2.740	1.46×10^{25}	0.866	1.60×10^{7}	3.21×10^{7}	0.499
FRB 20190714A	2.240	3.92×10^{24}	0.530	9.36×10^{6}	1.17×10^{7}	0.802
FRB 20191001A	2.220	3.57×10^{25}	0.922	1.30×10^{7}	4.17×10^{7}	0.311
FRB 20191228A	0.940	4.98×10^{24}	0.373	1.65×10^{6}	4.87×10^{6}	0.338
FRB 20200430A	1.491	5.60×10^{24}	0.383	3.95×10^{6}	5.27×10^{6}	0.749
FRB 20200627A	0.873	1.83×10^{24}	0.207	9.05×10^{5}	9.69×10^{5}	0.934
FRB 20200906A	2.768	2.18×10^{25}	0.585	1.40×10^{7}	1.56×10^{7}	0.900
FRB 20210117A	3.890	2.39×10^{25}	1.216	3.48×10^{7}	7.00×10^{7}	0.497
FRB 20210214G	1.575	2.27×10^{24}	0.411	4.38×10^{6}	5.97×10^{6}	0.734
FRB 20210320C	1.421	8.72×10^{24}	0.584	4.74×10^{6}	1.54×10^{7}	0.308
FRB 20210407E	11.853	8.86×10^{25}	3.045	1.74×10^{8}	2.52×10^{8}	0.693
FRB 20210807D	0.163	2.96×10^{23}	0.100	1.65×10^{4}	1.27×10^{5}	0.130
FRB 20210809C	2.213	1.33×10^{25}	0.577	9.33×10^{6}	1.33×10^{7}	0.699
FRB 20210912A	8.011	1.14×10^{26}	3.359	1.20×10^{8}	2.76×10^{8}	0.436
FRB 20211127I	0.506	8.73×10^{23}	0.220	3.48×10^{5}	1.21×10^{6}	0.286
FRB 20211203C	2.988	1.38×10^{25}	0.667	1.62×10^{7}	1.93×10^{7}	0.836

https://doi.org/10.1017/pasa.2024.114 Published online by Cambridge University Press

Table 4. (Continued)

Name	D_L (Gpc)	E_ν (J Hz^{-1})	z_{max} (Gpc)	$D_{L,max}$ (Gpc^3)	V_{max}	V/V_{max}
FRB 20211212A	0.432	2.44×10^{24}	0.285	2.58×10^5	2.29×10^6	0.113
FRB 20220105A	2.903	8.39×10^{24}	0.721	1.64×10^7	2.28×10^7	0.718
FRB 20220501C	1.923	7.65×10^{24}	0.517	7.51×10^6	1.14×10^7	0.660
FRB 20220531A	3.600	1.79×10^{25}	1.387	2.86×10^7	7.41×10^7	0.385
FRB 20220610A	9.979	9.70×10^{25}	2.939	1.49×10^8	2.45×10^8	0.609
FRB 20220725A	0.903	5.00×10^{24}	0.447	1.68×10^6	7.96×10^6	0.211
FRB 20220918A	3.299	2.91×10^{25}	1.416	2.59×10^7	8.15×10^7	0.318
FRB 20221106A	1.212	9.12×10^{24}	0.670	3.28×10^6	1.80×10^7	0.183
FRB 20230521A	3.171	1.70×10^{25}	0.779	1.91×10^7	2.64×10^7	0.724
FRB 20230526A	1.227	3.95×10^{24}	0.455	2.95×10^6	7.56×10^6	0.390
FRB 20230708A	1.545	1.88×10^{25}	0.805	5.64×10^6	2.69×10^7	0.210
FRB 20230731A	0.290	2.22×10^{23}	0.108	6.83×10^4	1.61×10^5	0.424
FRB 20230902A	1.835	5.11×10^{24}	0.441	6.34×10^6	7.89×10^6	0.803
FRB 20231006A	2.079	6.73×10^{24}	0.551	8.65×10^6	1.29×10^7	0.670
FRB 20231226A	1.105	7.63×10^{24}	0.602	2.71×10^6	1.51×10^7	0.179
FRB 20171020A*	0.00103	2.68×10^{22}	0.00050	0.00392	0.0177	0.222
FRB 20180430A*	0.00103	2.2×10^{22}	0.00048	0.00384	0.0154	0.249
FRB 20230718A*	0.00103	1.80×10^{18}	0.00028	0.00258	0.00292	0.882

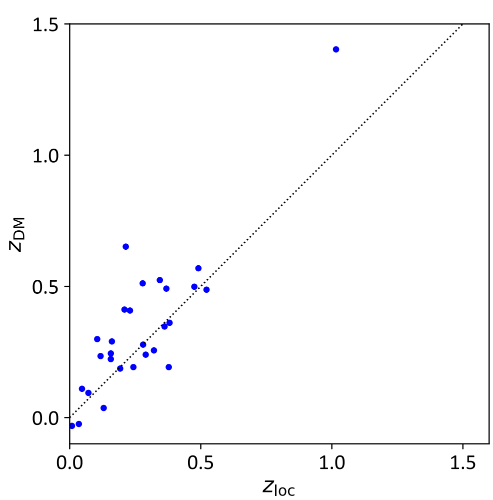

Figure 2. Scatter plot of spectroscopically measured host galaxy redshifts, z_{loc}, and those derived from the Macquart relation, z_{DM}, for the Localised High S/N Sample.

Full Sample contains no data in that luminosity bin. Such a low-energy excess has been observed in several repeating FRBs, with low-energy peaks becoming dominant in the $\sim +10^{22}-10^{23}$ J Hz^{-1} range (Niu et al. 2022b; Li et al. 2021). Furthermore, Kirsten et al. (2024) have found evidence for a flatter power-law index at energies above 10^{24}J Hz^{-1} for FRB 20201124A. This suggests that apparently once-off FRBs localised with ASKAP exhibit a qualitatively similar hardening of the RLF above 10^{23} J Hz^{-1}, though this is an ensemble average over the behaviour of many objects, and there are quantitative differences both within and between the RLFs measured for repeating FRBs; these samples may be subject to systematic biases, as discussed below.

4.2 Systematic biases – full sample

The Full Sample includes three low-DM FRBs with implied negative redshifts, which cannot therefore be trivially included in calculations. This results in the RLF that uses z_{DM} missing these events, which invariably occur in the nearby Universe, where under-fluctuations in DM_{Host}, DM_{Halo}, and/or DM_{MW} could result in low measured values of DM_{Obs}, such that only a negative value of z will satisfy equation (13). This effect can be seen most clearly in the missing data point for the Full Sample in the 10^{22}–10^{23} J Hz^{-1} bin in Fig. 4, which in the Localised High S/N Sample, is entirely due to FRB 20171020A. One method of avoiding such a bias is to marginalise over distributions of Milky Way and host galaxy DM contributions, as performed by Locatelli et al. (2019) – see Section 4.5 for further discussion of this approach.

The effect of this bias can be estimated by placing robust bounds on the true distance to these $z_{DM} < 0$ FRBs. A lower bound assumes they are not located in Local Group galaxies, limiting the luminosity distance $D_L \gtrsim 2$ Mpc (which equates to $z_{min} = 0.00024$, ignoring peculiar velocities). An upper bound assumes that the entire DM contribution is cosmological in nature, that is, $z_{max} = z_{DM}(DM_{cosmic} = DM_{Obs})$. We vary between these extremes, using $z = z_{min} + k(z_{max} - z_{min})$, for $k = 0, 0.1, 1.0$. We find that for $k \geq 0.2$, the effect on the RLF is negligible. However, for very low values of k, the RLF extends to very low luminosities, with a dependence $\propto E_\nu^{-1.5}$, since these FRBs invariably occupy the local Universe with approximately Euclidean geometry. The case of $k = 0$ only is shown in Fig. 5.

When assuming very nearby FRBs, the low-luminosity form of the RLF is significantly changed, and we are unable to obtain consistent fits. Excluding data below 10^{22} J Hz^{-1} produces almost identical values for γ and E_{max} as those previously found for the Full Sample. We therefore conclude that this bias limits our ability to probe the low-luminosity end of the RLF.

https://doi.org/10.1017/pasa.2024.114 Published online by Cambridge University Press

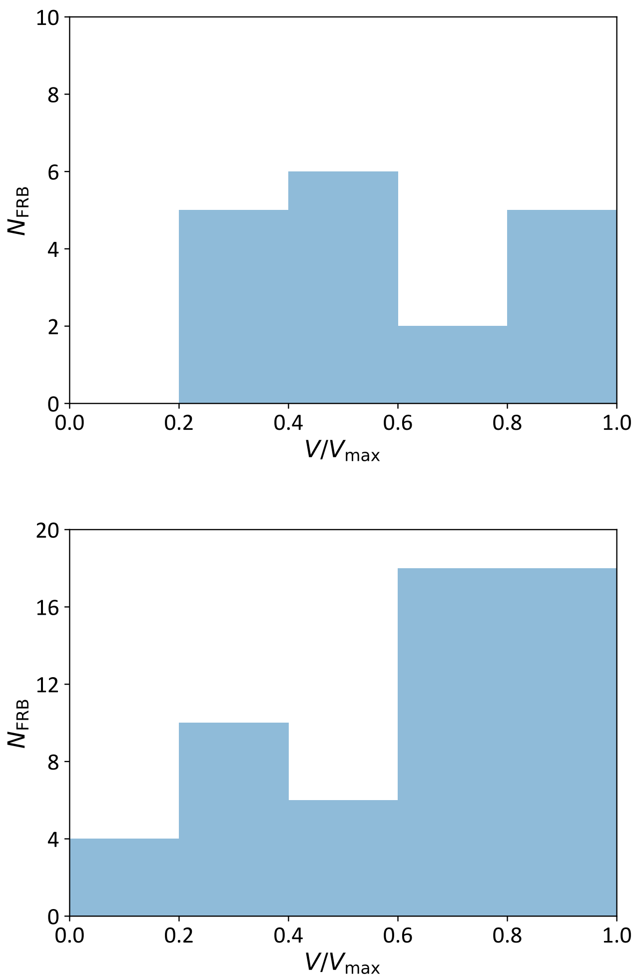

Figure 3. Histograms of $V/V_{\rm max}$ for both the Localised High S/N Sample (top) and Full Sample (bottom), under the assumption of no spectral dependence ($\alpha = 0$) or cosmological evolution ($n_{\rm SFR} = 0$). Three FRBs with negative $z_{\rm DM}$ values have been omitted from the Full Sample.

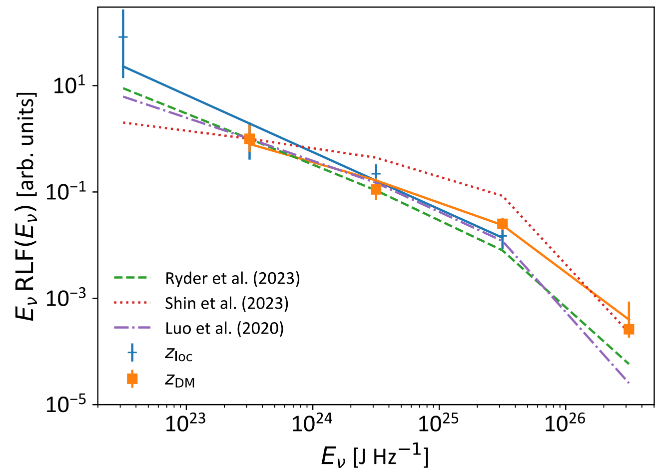

Figure 4. Radio luminosity functions (RLFs) calculated from the Localised High S/N Sample (using $z_{\rm loc}$) and Full Sample (using $z_{\rm DM}$). The (arbitrary) normalisation is fixed to unity at the 10^{23}–10^{24} bin. The best-fit Schechter functions for each sample are depicted for reference purposes. Also shown are luminosity functions derived from ASKAP and Parkes data by Ryder et al. (2023), CHIME data by Shin et al. (2023), and a mixed sample by Luo et al. (2020). The data are binned in log-space, so that the ordinate (y-axis) is effectively the RLF multiplied by the spectral fluence, E_ν.

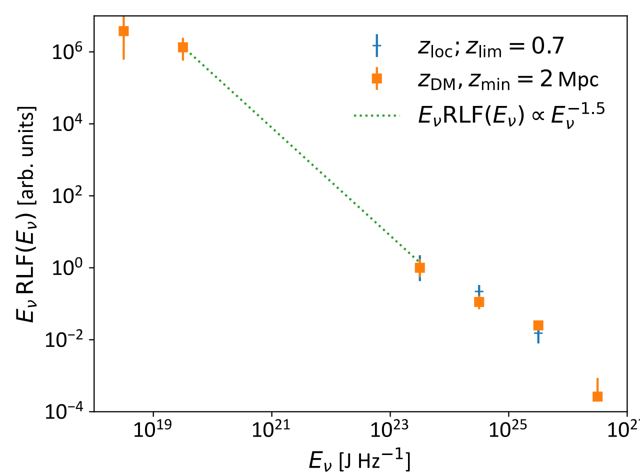

Figure 5. Data on radio luminosity functions (RLFs) calculated so as to account for observational biases, showing the full range allowing for a minimum distance at $z_{\rm min}$. The line indicating the E_ν RLF $\propto E_\nu^{-1.5}$ is to guide the eye only.

4.3 Systematic biases – localised high S/N sample

The inclusion of FRB 20171020A in the Localised High S/N Sample highlights our second source of systematic bias. FRB 20171020A only has a confident redshift precisely because it is nearby, thus its host galaxy can be identified despite the relatively large localisation errors of the CRAFT Fly's Eye observations. The analysis presented here has no means of accounting for the likely more-distant, higher-DM FRBs of the Fly's Eye sample (those from FRB 20170107A to FRB 20180525A) which cannot be included in the Localised High S/N Sample. A similar effect also occurs for high-redshift – and necessarily high-luminosity – FRBs, the host galaxies of which may be unidentifiable due to their large distance. An example of this is FRB 20210912A, where optical limits on the as-yet unseen host galaxy suggests $z > 0.7$, with $z = 1$ implying $E_\nu = 9.7 \cdot 10^{25}$ J Hz^{-1} in the case of $\alpha = 0$ (Marnoch et al. 2023). However, without this firm localisation, this undoubtedly energetic FRB cannot be included in the Localised High S/N Sample.

The biases mentioned above can be overcome in the case of the Localised High S/N Sample by using a limiting redshift $z_{\rm lim}$ such that all FRBs with $z < z_{\rm lim}$ are guaranteed to have their host galaxies identified. To do this, we first remove FRB 20171020A from the sample, since $z_{\rm lim}$ for the CRAFT Fly's Eye observations are poorly defined and set $z_{\rm lim} = 0.7$ for the remaining FRBs localised with ICS observations. All integrals over z in the calculations for V and $V_{\rm max}$ in Section 3 are then terminated at $z_{\rm lim}$, while FRBs located outside this volume are excluded. Thus, the definition of $V_{\rm max}$ becomes 'the volume within which this FRB would have been included in the analysis'. A limiting case of this method is to use only FRBs in a thin slice of redshift, between z and $z + dz$. In such a case, $V = V_{\rm max}$, and is constant for each and every FRB, such that every FRB has equal weight in the calculation of the luminosity function, consistent with expectation.

Fig. 5 shows the RLF for this updated sample of FRBs. It is only measured in the range 10^{23}–10^{25} J Hz^{-1}, and in this range,

https://doi.org/10.1017/pasa.2024.114 Published online by Cambridge University Press

Table 5. Mean $V/V_{\max}$ and best fit parameters (γ, $E_{\max}$) of the pure power-law and Schechter function fits to the FRB luminosity function for different data-sets, assuming no spectral dependence (i.e. $\alpha = 0$) or evolution of the source population. The p-values for the power-law fits are the probability of observing a χ^2 that value or higher should the power-law be the true model (high values indicate a good fit); for the Schechter function, the p-value is the probability of observing such a significant improvement in χ^2 should the power-law be the true model (low values are evidence for a Schechter function).

Sample	$\langle V/V_{\max}\rangle$	Function	γ	$\log_{10}(E_{\max})$	χ^2/ndf	p-value
Full sample	0.63	Power-law	-1.82 ± 0.12	N/A	4.24	0.01
		Schechter	-1.69 ± 0.15	25.8 ± 0.39	2.2	0.34
De-biased Full Sample* ($z = z_{\min}$)	0.62	Power-law	-1.81 ± 0.11	N/A	3.64	0.03
		Schechter	-1.69 ± 0.15	25.8 ± 0.44	2.13	0.36
Localised High S/N Sample	0.58	Power-law	-2.11 ± 0.18	N/A	6.15	0.00
		Schechter	$-2.11+^{\#\#}$	40.5	3.1	0.34
De-biased Localised High S/N Sample $z_{\max} = 0.7$	0.61	Power-law	-1.96 ± 0.15	N/A	2.84	0.09
		Schechter	$-1.58^{\#}$	$25.1^{\#}$	#	#

*Assumes FRBs with a negative z_{DM} are located at a distance of $z_{\min} = 0.00024$ (2 Mpc); fit excludes data below 10^{22} J Hz^{-1}.
#No errors can be estimated for these parameters, due to the number of degrees of freedom (ndf.) of the fit being zero.
##The best-fit value of $E_{\max}$ is effectively infinite, rendering error calculations for the parameters meaningless.

is consistent with a pure power-law with slope $\gamma = -1.96 \pm 0.15$ (p-value of linear fit 0.09); a Schechter function produces a much flatter differential slope $\gamma = -1.58$ and turn-over energy of $E_{\max} = 1.2 \times 10^{25}$ J Hz^{-1} (errors cannot be estimated since the number of variables equals the number of points, i.e. it is statistically ill-posed).

4.4 Comparison with other results

Fits of the FRB RLF have been undertaken by several authors. While many assume a 1:1 z–DM relation, we concentrate on those which have fully modelled uncertainties in FRB redshift given DM, and/or used a sample of localised FRBs, while accounting for selection effects as per Connor (2019). Luo et al. (2020) uses a mixed sample of mostly unlocalised FRBs from several instruments – including Parkes and ASKAP – to fit a Schechter function with differential index $\gamma = -1.79^{+0.31}_{-0.35}$ and $E_{\max} = 2.9^{+11.9}_{-1.7} \cdot 10^{25}$J Hz^{-1} (assuming a 1 ms burst width and 1 GHz bandwidth). James et al. (2022) uses a sample of 16 FRBs with host redshifts, and approximately 60 without, to find an index of $-1.95^{+0.18}_{-0.15}$, with Ryder et al. (2023) updating $E_{\max}$ to $5^{+3}_{-2} \cdot 10^{25}$J Hz^{-1}. Shin et al. (2023) fits the dispersion measure of 536 FRBs observed by CHIME to find an index of $-1.3^{+0.7}_{-0.4}$ and $E_{\max} = 2.38^{+5.65}_{-1.64} \cdot 10^{25}$J Hz^{-1}. These results are broadly consistent with the range of RLFs derived in this work, although they would have difficulty fitting the possible low-energy excess observed in the potentially biased Localised High S/N Sample, and the fit of Shin et al. (2023) is flatter, and has a downturn which is stronger, than allowed by our data. We note that James et al. (2022) accounts for the biases discussed in Section 4.2 by not using the localisation of FRB 20171020A or FRBs above $\mathrm{DM_{EG}}$ of 1 000 pc cm^{-3}, while Shin et al. (2023) fits FRBs at lower frequency which may have a different underlying RLF. The possible minimum energy (or downturn) at $23.47^{0.54}_{-1.28}$ J Hz^{-1} suggested by Hoffmann et al. (2024a) is not observed, but lies at the lower end of the RLF which we can probe. We therefore conclude that, given uncertainties in FRB spectral behaviour and source evolution, and possible biased effects in our own analysis, we cannot discriminate between these previous fits.

4.5 Comparison with Locatelli et al. (2019)

Locatelli et al. (2019) also apply the $V/V_{\max}$ test to FRBs by comparing 23 FRBs discovered by ASKAP with 20 of the FRBs found by Parkes up to 2019. Their paper focuses on the use of the $V/V_{\max}$ distribution to explore evolution, while our paper uses the $V_{\max}$ method to estimate the luminosity distribution. These are different uses, and analysis of $V/V_{\max}$ needs complete unbiased samples which is quite problematic for FRBs as discussed in Section 4.3. They find evidence for cosmological source evolution in the ASKAP sample, with $\langle V/V_{\max}\rangle = 0.68 \pm 0.05$, but less so for the Parkes data, with $\langle V/V_{\max}\rangle = 0.54 \pm 0.04$, assuming a spectral evolution of $\alpha = 1.6$.

For ASKAP, Locatelli et al. (2019) only analyse the ICS sample, which was all that was available at the time. They also include the Parkes FRB sample; however, for these FRBs the location in the beam is not known, so neither $V_{\max}$ nor the actual beam-corrected fluences are known; we therefore excluded the Parkes FRB sample in our analysis. This difficulty will also apply to the much larger CHIME sample. The authors also omit discussion of beam areas for Parkes and ASKAP.

As discussed in Section 4.2, Locatelli et al. (2019) builds appropriate probability functions to estimate the redshift PDF(z) instead of using a unique value. This treatment is an elegant way to avoid the bias due to negative apparent redshifts encountered when only the mean DM correction is used. We note that the ZDM code is able to produce such PDFs, for example, as per Lee-Waddell et al. (2023).

Our results for $\langle V/V_{\max}\rangle$ for the Localised High S/N Sample and Full Sample are 0.58 and 0.63, respectively (0.61 and 0.62 when debiased); when we include a spectral dependence of $\alpha = -1.5$ (see Appendix A), we find $\langle V/V_{\max}\rangle = 0.67$ for the Full Sample, consistent with the result of Locatelli et al. (2019).

5. Conclusions

We have shown how to apply the $V/V_{\max}$ method of Schmidt (1968) to a population of transient sources and applied this to FRBs. We find that the current sample of FRBs detected by ASKAP/CRAFT is insufficient to distinguish between competing

https://doi.org/10.1017/pasa.2024.114 Published online by Cambridge University Press

evolutionary and spectral models, with the greatest departure from uniformity in the $V/V_{\rm max}$ distribution being due to a dearth of very high S/N FRBs.

Using both FRBs with known redshift, $z_{\rm loc}$, and a larger sample of FRBs with $z_{\rm DM}$ estimated from the Macquart relation, we plot the FRB energy distribution in the range 10^{23}–10^{26} J Hz^{-1}. We find it to be fairly consistent ($p = 0.09$) with a power-law with differential slope $\gamma = -1.96 \pm 0.15$ using $z_{\rm loc}$. Above this energy, we find some evidence of a downturn consistent with a Schechter function with $E_{\rm max} = 6.3 \times 10^{25}$ when using $z_{\rm DM}$. We have also identified several systematic effects in the analysis and shown how to take these into account. In particular, the difficulty of identifying high-z host galaxies limits our knowledge of the tip of the FRB energy distribution, as it is unclear if the downturn in the energy distribution seen in the $z_{\rm DM}$ result is physical, or an artefact of smearing in the Macquart relation.

In the near future, FRB surveys will detect too many bursts to follow up their host galaxies individually with 8 m-class telescope time (e.g. CHORD; Vanderlinde et al. 2019). Low-DM, near-Universe host galaxies can likely be identified in existing or impending (e.g. LSST) optical surveys without further follow-up, allowing an unbiased sample of the $E_\nu < 10^{23}$ J Hz^{-1} region to be formed. Moreover, we find that the use of $z_{\rm DM}$ compared to $z_{\rm loc}$ does not significantly affect the luminosity function in the range 10^{23}–10^{26} J Hz^{-1}. We therefore recommend that optical follow-up time be focused on identifying high-DM/$z_{\rm loc}$ FRBs, to allow the high-end of the FRB luminosity function to be studied.

Acknowledgement. This scientific work uses data obtained from Inyarrimanha Ilgari Bundara/the Murchison Radio-astronomy Observatory. We acknowledge the Wajarri Yamaji People as the Traditional Owners and native title holders of the Observatory site. CSIRO's ASKAP radio telescope is part of the Australia Telescope National Facility (https://ror.org/05qajvd42). Operation of ASKAP is funded by the Australian Government with support from the National Collaborative Research Infrastructure Strategy. ASKAP uses the resources of the Pawsey Supercomputing Research Centre. Establishment of ASKAP, Inyarrimanha Ilgari Bundara, the CSIRO Murchison Radio-astronomy Observatory and the Pawsey Supercomputing Research Centre are initiatives of the Australian Government, with support from the Government of Western Australia and the Science and Industry Endowment Fund.

Funding statement. W.A. acknowledges the contribution of an Australian Government Research Training Program Scholarship in support of this research. C.W.J. and M.G. acknowledge support by the Australian Government through the Australian Research Council's Discovery Projects funding scheme (project DP 210102103). A.T.D. and R.M.S. acknowledge support through ARC Discovery Project DP 220102305. R.M.S. acknowledges support through ARC Discovery Project DP 220102305. This research was supported by the Australian Research Council Centre of Excellence for All Sky Astrophysics in 3 Dimensions (ASTRO 3D) through project no. CE 170100013. A.C.G. and the Fong Group at Northwestern acknowledges support by the National Science Foundation under grant Nos. AST-1909358, AST-2308182 and CAREER grant No. AST-2047919. A.C.G. acknowledges support from NSF grants AST-1911140, AST-1910471 and AST-2206490 as a member of the Fast and Fortunate for FRB Follow-up team.

Competing interests. None.

Data availability statement. Data underlying this article are available within this article. Code to generate $V/V_{\rm max}$ and luminosity functions is contained in the FRB repository (James, Prochaska, & Ghosh 2021b). Digitised versions of the figures are available upon reasonable request to the authors.

References

Abdalla, E., et al. 2022, JHEA, 34, 49. https://doi.org/10.1016/j.jheap.2022.04.002. arXiv: 2203.06142 [astro-ph.CO].
Agarwal, D., et al. 2019, MNRAS, 490, 1. https://doi.org/10.1093/mnras/stz2574. arXiv: 1909.05779 [astro-ph.HE].
Arcus, W. R., James, C. W., Ekers, R. D., & Wayth, R. B. 2022, MNRAS, 512, 2093. Issu: 0035-8711. https://doi.org/10.1093/mnras/stac626. eprint: https://academic.oup.com/mnras/article-pdf/512/2/2093/43030556/stac626.pdf
Arcus, W. R., Macquart, J.-P., Sammons, M. W., James, C. W., & Ekers, R. D. 2020, MNRAS, 501, 5319. Issu: 0035-8711. https://doi.org/10.1093/mnras/staa3948. eprint: https://academic.oup.com/mnras/article-pdf/501/4/5319/35934130/staa3948.pdf
Avni, Y., & Bahcall, J. N. 1980, ApJ, 235, 694. https://doi.org/10.1086/157673.
Bannister, K. W., et al. 2019, Sci, 365, 565. https://doi.org/10.1126/science.aaw5903. arXiv: 1906.11476 [astro-ph.HE].
Bannister, K. W., et al. 2017, ApJ, 841, L12. https://doi.org/10.3847/2041-8213/aa71ff. arXiv:1705.07581 [astro-ph.HE].
Baptista, J., et al. 2024, ApJ, 965, 57. https://doi.org/10.3847/1538-4357/ad2705. arXiv: 2305.07022 [astro-ph.CO].
Best, P. N., Kauffmann, G., Heckman, T. M., Brinchmann, J., Charlot, S., Ivezić, Ž., & White, S. D. M. 2005, MNRAS, 362, 25. https://doi.org/10.1111/j.1365-2966.2005.09192.x. arXiv: astro-ph/0506269 [astro-ph].
Bhandari, S., Bannister, K. W., James, C. W., Shannon, R. M., Flynn, C. M., Caleb, M., & Bunton, J. D. 2019, MNRAS, 486, 70. https://doi.org/10.1093/mnras/stz804. arXiv: 1903.06525 [astro-ph.HE].
Bhandari, S., et al. 2020, ApJ, 901, L20. https://doi.org/10.3847/2041-8213/abb462. arXiv: 2008.12488 [astro-ph.HE].
Bhandari, S., et al. 2023, ApJ, 948, 67. https://doi.org/10.3847/1538-4357/acc178. arXiv: 2211.16790 [astro-ph.HE].
Bhandari, S., et al. 2022, AJ, 163, 69. https://doi.org/10.3847/1538-3881/ac3aec. arXiv: 2108.01282 [astro-ph.HE].
Bhardwaj, M., et al. 2021, ApJ, 910, L18. https://doi.org/10.3847/2041-8213/abeaa6. arXiv: 2103.01295 [astro-ph.HE].
Cao, X.-F., Yu, Y.-W., & Zhou, X. 2018, ApJ, 858, 89. https://doi.org/10.3847/1538-4357/aabadd. arXiv: 1803.06266 [astro-ph.HE].
Chatterjee, S., et al. 2017, Natur, 541, 58. https://doi.org/10.1038/nature20797. arXiv: 1701.01098 [astro-ph.HE].
CHIME/FRB Collaboration, et al. 2021, ApJS, 257, 59. https://doi.org/10.3847/1538-4365/ac33ab. arXiv: 2106.04352 [astro-ph.HE].
Condon, J. J., Cotton, W. D., & Broderick, J. J. 2002, AJ, 124, 675. https://doi.org/10.1086/341650.
Connor, L. 2019, MNRAS, 487, 5753. https://doi.org/10.1093/mnras/stz1666. arXiv: 1905.00755 [astro-ph.HE].
Cordes, J. M., & Lazio, T. J. W. 2003, arXiv: astro-ph/0301598 [astro-ph].
Cordes, J. M., & McLaughlin, M. A. 2003, ApJ, 596, 1142. https://doi.org/10.1086/378231. eprint: astro-ph/0304364.
Deng, W., & Zhang, B. 2014, ApJ, 783, L35. https://doi.org/10.1088/2041-8205/783/2/L35. arXiv: 1401.0059 [astro-ph.HE].
Dunlop, J. S., & Peacock, J. A. 1990, MNRAS, 247, 19.
Farah, W., et al. 2019, MNRAS, 488, 2989. https://doi.org/10.1093/mnras/stz1748. arXiv: 1905.02293 [astro-ph.HE].
Gordon, A. C., et al. 2024, ApJ, 963, L34. https://doi.org/10.3847/2041-8213/ad2773.
Hashimoto, T., et al. 2022, MNRAS, 511, 1961. https://doi.org/10.1093/mnras/stac065. arXiv: 2201.03574 [astro-ph.HE].
Heintz, K. E., et al. 2020, ApJ, 903, 152. https://doi.org/10.3847/1538-4357/abb6fb. arXiv: 2009.10747 [astro-ph.GA].

Hoffmann, J., et al. 2024a, MNRAS, 528, 1583. https://doi.org/10.1093/mnras/stae131. arXiv: 2408.05937 [astro-ph.HE].
Hoffmann, J., James, C. W., Glowacki, M., Prochaska, J. X., Gordon, A. C., Deller, A. T., Shannon, R. M., & Ryder, S. D. 2024b, arXiv: 2408.04878 [astro-ph.CO].
Hotan, A. W., et al. 2021, PASA, 38, e009. https://doi.org/10.1017/pasa.2021.1. arXiv: 2102.01870 [astro-ph.IM].
Inoue, S. 2004, MNRAS, 348, 999. https://doi.org/10.1111/j.1365-2966.2004.07359.x. eprint: astro-ph/0309364.
Ioka, K. 2003, ApJ, 598, L79. https://doi.org/10.1086/380598. arXiv: astro-ph/0309200 [astro-ph].
James, C. W., Prochaska, J. X., Macquart, J.-P., North-Hickey, F. O., Bannister, K. W., & Dunning, A. 2021a, MNRAS, 509, 4775. https://doi.org/10.1093/mnras/stab3051
James, C. W., et al. 2019, PASA, 36, e009. https://doi.org/10.1017/pasa.2019.1. arXiv: 1810.04356 [astro-ph.HE].
James, C. W., et al. 2022, MNRAS, 516, 4862. https://doi.org/10.1093/mnras/stac2524. arXiv: 2208.00819 [astro-ph.CO].
James, C. W., Prochaska, J. X., & Ghosh, E. M. 2021b, *Zdm*. V. 0.1, August 18, 2021.
Keane, E. F., et al. 2018, MNRAS, 473, 116. https://doi.org/10.1093/mnras/stx2126. arXiv: 1706.04459 [astro-ph.IM].
Keane, E. F., & Petroff, E. 2015, MNRAS, 447, 2852. https://doi.org/10.1093/mnras/stu2650. arXiv: 1409.6125 [astro-ph.HE].
Keating, L. C., & Pen, U.-L. 2020, MNRAS, 496, L106. https://doi.org/10.1093/mnrasl/slaa095. arXiv: 2001.11105 [astro-ph.GA].
Kirsten, F., et al. 2024, NatAs. https://doi.org/10.1038/s41550-023-02153-z. arXiv: 2306.15505 [astro-ph.HE].
Law, C. J., et al. 2018, ApJS, 236, 8. https://doi.org/10.3847/1538-4365/aab77b. arXiv: 1802.03084 [astro-ph.IM].
Law, C. J., et al. 2024, ApJ, 967, 29. https://doi.org/10.3847/1538-4357/ad3736. arXiv: 2307.03344 [astro-ph.HE].
Lee-Waddell, K., et al. 2023, PASA, 40, e029. https://doi.org/10.1017/pasa.2023.27. arXiv: 2305.17960 [astro-ph.GA].
Leung, C., et al. 2021, AJ, 161, 81. https://doi.org/10.3847/1538-3881/abd174. arXiv: 2008.11738 [astro-ph.IM].
Li, D., et al. 2021, Natur, 598, 267. https://doi.org/10.1038/s41586-021-03878-5. arXiv: 2107.08205 [astro-ph.HE].
Locatelli, N., Ronchi, M., Ghirlanda, G., & Ghisellini, G. 2019, A&A, 625, A109. https://doi.org/10.1051/0004-6361/201834722. arXiv: 1811.10641 [astro-ph.HE].
Lorimer, D. R., Bailes, M., McLaughlin, M. A., Narkevic, D. J., & Crawford, F. 2007, Sci, 318, 777. https://doi.org/10.1126/science.1147532. arXiv: 0709.4301.
Lu, W., & Piro, A. L. 2019, ApJ, 883, 40. https://doi.org/10.3847/1538-4357/ab3796. arXiv: 1903.00014 [astro-ph.HE].
Luo, R., Men, Y., Lee, K., Wang, W., Lorimer, D. R., & Zhang, B. 2020, MNRAS, 494, 665. https://doi.org/10.1093/mnras/staa704. arXiv: 2003.04848 [astro-ph.HE].
Macquart, J.-P., & Ekers, R. D. 2018a, MNRAS, 474, 1900. https://doi.org/10.1093/mnras/stx2825. arXiv: 1710.11493 [astro-ph.HE].
Macquart, J.-P., & Ekers, R. D. 2018b, MNRAS, 480, 4211. https://doi.org/10.1093/mnras/sty2083. arXiv: 1808.00908 [astro-ph.HE].
Macquart, J.-P., et al. 2020, Natur, 581, 391. https://doi.org/10.1038/s41586-020-2300-2. arXiv: 2005.13161 [astro-ph.CO].
Macquart, J.-P., Shannon, R. M., Bannister, K. W., James, C. W., Ekers, R. D., & Bunton, J. D. 2019, ApJ, 872, L19. https://doi.org/10.3847/2041-8213/ab03d6. arXiv: 1810.04353 [astro-ph.HE].
Macquart, J.-P., et al. 2010, PASA, 27, 272. https://doi.org/10.1071/AS09082. arXiv: 1001.2958 [astro-ph.HE].
Madau, P., & Dickinson, M. 2014, ARA&A, 52, 415. https://doi.org/10.1146/annurev-astro-081811-125615. arXiv: 1403.0007.
Mahony, E. K., et al. 2018, ApJ, 867, L10. https://doi.org/10.3847/2041-8213/aae7cb
Marnoch, L., et al. 2023, MNRAS, 525, 994. https://doi.org/10.1093/mnras/stad2353. arXiv: 2307.14702 [astro-ph.HE].
Mauch, T., & Sadler, E. M. 2007, MNRAS, 375, 931. https://doi.org/10.1111/j.1365-2966.2006.11353.x. arXiv: astro-ph/0612018 [astro-ph].
Merryfield, M., et al. 2023, AJ, 165, 152. https://doi.org/10.3847/1538-3881/ac9ab5. arXiv: 2206.14079 [astro-ph.IM].
Niu, C.-H., et al. 2021, ApJ, 909, L8. https://doi.org/10.3847/2041-8213/abe7f0. arXiv: 2102.10546 [astro-ph.HE].
Niu, C.-H., et al. 2022a, Natur, 606, 873. https://doi.org/10.1038/s41586-022-04755-5. arXiv: 2110.07418 [astro-ph.HE].
Niu, J.-R., et al. 2022b, RAA, 22, 124004. https://doi.org/10.1088/1674-4527/ac995d. arXiv: 2210. 03610 [astro-ph.HE].
Oppermann, N., Connor, L. D., & Pen, U.-L. 2016, MNRAS, 461, 984. https://doi.org/10.1093/mnras/stw1401. arXiv: 1604.03909 [astro-ph.HE].
Petroff, E., Hessels, J. W. T., & Lorimer, D. R. 2022, A&AR, 30, 2. https://doi.org/10.1007/s00159-022-00139-w. arXiv: 2107.10113 [astro-ph.HE].
Planck Collaboration, et al. 2016, A&A, 594, A13.
Pracy, M. B., et al. 2016, MNRAS, 460, 2. https://doi.org/10.1093/mnras/stw910. arXiv: 1604.04332 [astro-ph.GA].
Prochaska, J. X., Simha, S., Law, C., Tejos, N., & Neeleman, M. 2019a, Frb. V. 1.0.0, September 10, 2019.
Prochaska, J. X., et al. 2019b, Sci, 366, 231. https://doi.org/10.1126/science.aay0073
Prochaska, J. X., & Zheng, Y. 2019, MNRAS, 485, 648. https://doi.org/10.1093/mnras/stz261. arXiv: 1901.11051 [astro-ph.GA].
Qiu, H., Bannister, K. W., Shannon, R. M., Murphy, T., Bhandari, S., Agarwal, D., Lorimer, D. R., & Bunton, J. D. 2019, MNRAS, 486, 166. https://doi.org/10.1093/mnras/stz748. arXiv: 1903.04694 [astro-ph.HE].
Qiu, H., Keane, E. F., Bannister, K. W., James, C. W., & Shannon, R. M. 2023, MNRAS, 523, 5109. https://doi.org/10.1093/mnras/stad1740. arXiv: 2306.03886 [astro-ph.IM].
Rajwade, K. M., et al. 2022, MNRAS, 514, 1961. https://doi.org/10.1093/mnras/stac1450. arXiv: 2205.14600 [astro-ph.HE].
Ryder, S. D., et al. 2023, Sci, 382, 294. https://doi.org/10.1126/science.adf2678. arXiv: 2210.04680 [astro-ph.HE].
Sadler, E. M., et al. 2002, MNRAS, 329, 227. https://doi.org/10.1046/j.1365-8711.2002.04998.x. arXiv: astro-ph/0106173 [astro-ph].
Schmidt, M. 1963, Natur, 197, 1040
Schmidt, M. 1968, ApJ, 151, 393. https://doi.org/doi:10.1086/149446.
Schmidt, M. 2009, ApJ, 700, 633. https://doi.org/10.1088/0004-637X/700/1/633. arXiv: 0905.2968 [astro-ph.CO].
Schnitzeler, D. H. F. M. 2012, MNRAS, 427, 664. https://doi.org/10.1111/j.1365-2966.2012.21869.x. arXiv: 1208.3045 [astro-ph.GA].
Shannon, R. M., et al. 2024, https://doi.org/10.48550/arXiv.2408.02083.
Shannon, R. M., et al. 2018, Natur, 562, 386. https://doi.org/10.1038/s41586-018-0588-y.
Shin, K., et al. 2023, ApJ, 944, 105. https://doi.org/10.3847/1538-4357/acaf06. arXiv: 2207.14316 [astro-ph.HE].
Thornton, D., et al. 2013, Sci, 341, 53. https://doi.org/10.1126/science.1236789. arXiv: 1307.1628 [astro-ph.HE].
Vanderlinde, K., et al. 2019, in Canadian Long Range Plan for Astronomy and Astrophysics White Papers, 2020, 28. https://doi.org/10.5281/zenodo.3765414. arXiv: 1911.01777 [astro-ph.IM].
Zhang, J.-G., Li, Y., Zou, J.-M., Zhao, Z.-W., Zhang, J.-F., & Zhang, X. 2024, Universe, 10, 207. https://doi.org/10.3390/universe10050207. arXiv: 2303.16775 [astro-ph.HE].

Appendix A. Investigation of Spectral Dependence and Source Evolution

For simplicity, in the main body of this work, we treated the case of no spectral dependence and no cosmological source evolution. Here, we show that with current data, the $V/V_{\rm max}$ test cannot determine whether either effect is present, and show the resulting systematic effects on the luminosity function.

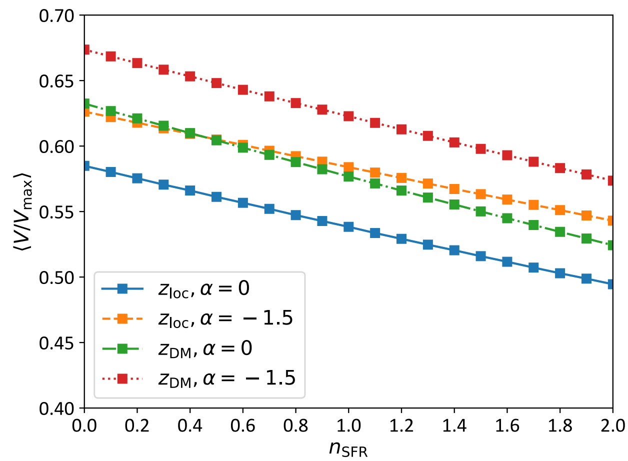

Figure A1. Calculated values of $\langle V/V_{\rm max}\rangle$, considering two values of the spectral index $\alpha = \{0, -1.5\}$, for both the Localised High S/N Sample (using $z_{\rm loc}$) and the Full Sample (using $z_{\rm DM}$), as a function of the star formation rate scaling parameter $n_{\rm SFR}$.

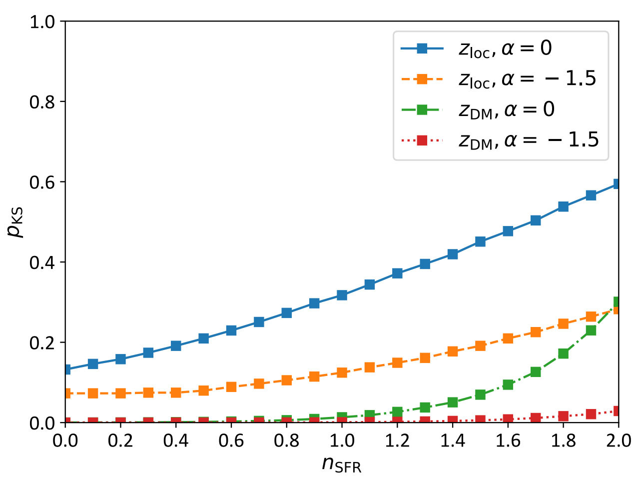

Figure A2. *P*-values resulting from the KS-test for uniformity in $V/V_{\rm max}$, considering two values of the spectral index $\alpha = \{0, -1.5\}$, for both the Localised High S/N Sample (using $z_{\rm loc}$) and the Full Sample (using $z_{\rm DM}$), as a function of the star formation rate scaling parameter $n_{\rm SFR}$.

The spectral dependence of FRBs is still uncertain. Macquart et al. (2019) used ASKAP FRBs to determine a spectral dependence of $F_\nu \propto \nu^\alpha$, with $\alpha = -1.5^{+0.2}_{-0.3}$, though as noted by James et al. (2021a), selection biases due to FRBs being narrow-band might imply the true dependence is $\alpha = -0.65$. The apparent rate of FRBs measured by CHIME appears to be frequency-independent; however as noted by the authors, this does not account for selection biases (CHIME/FRB Collaboration: Amiri et al. 2021). Population modelling by James et al. (2022) and Shin et al. (2023) find some evidence for increased spectral strength at lower frequencies, however constraints are very weak, as are those from studies of the frequency-dependent detection rate measured by ASKAP. We therefore consider both $\alpha = 0$ and $\alpha = -1.5$ in this investigation.

The source evolution function, ψ, weights the physical volume, V, to produce an effective volume, V'. If the source density in the Universe varies with redshift, then only the distribution of $V'/V_{\rm max}{}'$ will be uniform between 0 and 1. The source evolution function $\psi(z)$ is inserted into the integrals over redshift, viz., equations (11) and (12) to calculate $V'_{\rm max}$ and V', respectively. Since $V' = V$ only in the case that the FRB population does not cosmologically evolve – a situation which we do not deem likely – we henceforth drop the $'$ notation so that both V and $V_{\rm max}$ are implicitly understood to be weighted by $\psi(z)$.

We consider source evolution by scaling V to some power of the star formation rate as parameterised by Madau & Dickinson (2014), A

$$\mathrm{SFR}(z) \propto \frac{(1+z)^{2.7}}{1+\left(\frac{1+z}{2.9}\right)^{5.6}}, \tag{A1}$$

$$\psi(z) = (\mathrm{SFR}(z))^{n_{\rm SFR}}. \tag{A2}$$

Given that the majority of this sample represents the $z < 0.5$ Universe, where the denominator of equation (A1) changes by at most 2.5%, this scaling is almost equivalent to a scaling of $\psi(z) = (1+z)^{2.7 n_{\rm SFR}}$. A

Fig. A1 plots the $\langle V/V_{\rm max}\rangle$ values for both the Localised High S/N Sample and Full Sample along with their 95% confidence intervals, determined using the bootstrap method described in Appendix C. To check for population uniformity, we further conduct a Kolmogorov-Smirnoff (K-S)-test with respect to a uniform distribution for both samples. The resulting *p*-values are shown in Fig. A2.

A.1 Uniformity of $V/V_{\rm max}$

Varying both α and $n_{\rm SFR}$ produces our results on the uniformity of $V/V_{\rm max}$ shown in Figs. A1–A3. Requiring only that $\langle V/V_{\rm max}\rangle = 0.5$ favours a strongly evolving FRB population, with $n_{\rm SFR} = 1.7$ for $\alpha = 0$, and $n_{\rm SFR} > 2$ for $\alpha = -1.5$. Both the Localised High S/N Sample and Full Sample yield almost identical values of $\langle V/V_{\rm max}\rangle$. The *p*-values of the KS-statistics shown in Fig. A2 confirm this, however at the 2σ level ($p < 0.05$), no value of $n_{\rm SFR}$ is excluded for the Localised High S/N Sample, while the Full Sample shows stronger evidence against uniformity for low $n_{\rm SFR}$.

The driver of these results, as shown in Fig. A3, is the lack of events with very low $V/V_{\rm max}$ – equivalently, a lack of very high S/N events. Indeed, none of the cumulative $V/V_{\rm max}$ distributions give a very good fit to uniformity. We have considered in Shannon et al. (in preparation) whether or not this effect could be due to instrumental bias, and concluded that high S/N events would still be detectable in adjacent beams even if a primary beam was saturated. We therefore conclude that the lack of low $V/V_{\rm max}$ events is probably a statistical under-fluctuation, and that uniformity in $\langle V/V_{\rm max}\rangle$ does not currently discriminate between different values of $n_{\rm SFR}$ and α. Fig. A3 also illustrates the degeneracy between $n_{\rm SFR}$ and α: a steeper spectral index, and hence k-correction, allows for a more strongly evolving source population, as noted by James et al. (2021a).

Our inability to distinguish between plausible values of α and $n_{\rm SFR}$ results in a difference in the behaviour of the luminosity functions at high energies, as shown in Fig. A4. No spectral evolution ($\alpha = 0$) predicts distributions consistent with a pure power-law, while $\alpha = -1.5$ produces a high-energy downturn consistent with the Schechter function. The effect of increasing $n_{\rm SFR}$ is primarily to produce a stronger downturn (lower $E_{\rm max}$), though this is only evident for $\alpha = -1.5$.

https://doi.org/10.1017/pasa.2024.114 Published online by Cambridge University Press

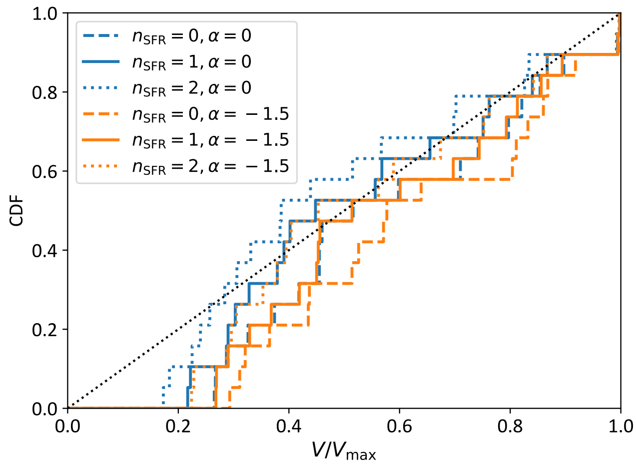

Figure A3. Cumulative histograms of V/V_{max} for six combinations of α and n_{SFR} for the Localised High S/N Sample, compared to the expectation (black dotted line). Note that the $n_{SFR} = 0, \alpha = 0$ and $n_{SFR} = 1, \alpha = -1.5$ plots almost overlap, as do the $n_{SFR} = 1, \alpha = 0$ and $n_{SFR} = 2, \alpha = -1.5$ plots.

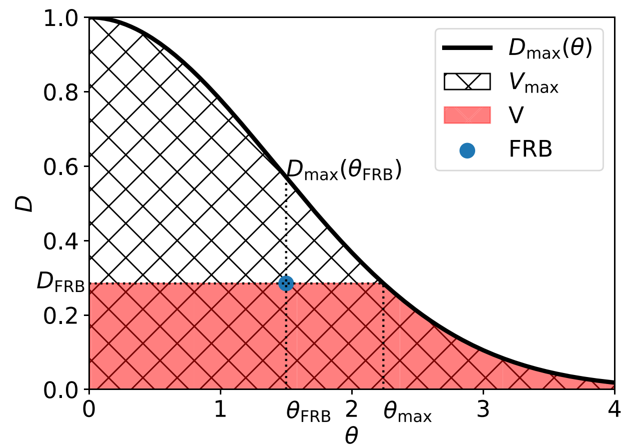

Figure B1. Illustration of the volumes V and V_{max} for an FRB detected at distance D_{FRB} at position θ_{FRB} away from the beam centre.

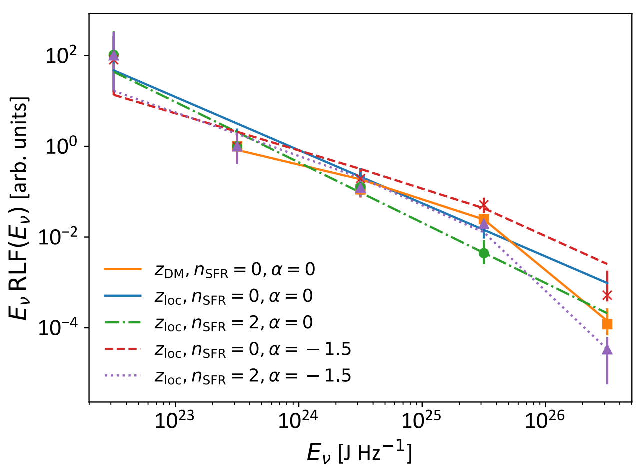

Figure A4. Radio luminosity functions (RLFs) calculated from the Localised High S/N Sample (using z_{loc}) for combinations of $\alpha = \{0, -1.5\}$ and $n_{SFR} = \{0, 2\}$, and from the Full Sample (using z_{DM}) for $\alpha = 0$, $n_{SFR} = 0$. The (arbitrary) normalisation is fixed to unity at the 10^{23}–10^{24} bin. The best-fit Schechter functions for each sample are depicted for reference purposes.

The uncertainty in the luminosity function, due to our inability to determine the population evolution or the spectral dependence with V/V_{max}, is comparable to the systematic errors identified in the Full Sample and Localised High S/N Sample discussed in Section 4.2. However, this method could be used to constrain these parameters in a future analysis.

Appendix B. Using V/V_{max} with Non-uniform Sensitivity

The original formulation of the V/V_{max}-test by Schmidt (1968) was provided in the context of optical and radio quasar surveys with well-defined luminosity thresholds, S_{cutoff}, and survey areas, Ω. This allowed for conceptually easy definitions of survey volumes V and V_{max} for a given cosmology. For transient sources such as FRBs however, the definition of these quantities becomes less obvious. Here we show how to construct V and V_{max} in the case of spatial- and time-varying sensitivity.

Appendix B.1. Spatially Varying Sensitivity

FRBs are transients, and as such they will be observed at a particular part of a telescope's beam, with sensitivity, B, with respect to the beam centre (where $B = 1$). Unlike steady sources, where multiple pointings can, to a large extent, correct for sources viewed far from the beam centre, S_{cutoff} – or in our formulation, $F_{\nu,cutoff}$ – varies over solid angle, hence from event-to-event. While this approach generalises to any spatially varying sensitivity, we consider only the beamshape B, where $F_{\nu,cutoff} \propto B^{-1}$, hereinafter.

One approach (a differential method) to deal with this is to consider only an infinitesimal solid angle, $d\Omega$, about the point of detection. In this case, the fluence cutoff, $F_{\nu,cutoff}$, is well-defined since the beam sensitivity is locally constant. Each and every detection therefore becomes its own survey over an infinitesimal solid angle $d\Omega$, resulting in infinitesimally small $V \to dV$ and $V_{max} \to dV_{max}$. In such a case, the absolute values of dV and dV_{max} have little meaning, preventing the total source density from being derived; their ratio, however, is well-defined and preserves the properties of the V/V_{max}-test. B

An alternative approach (an integral method) is to consider the total volume viewed by the telescope beam and the regions over which the FRB could have been detected. This situation is illustrated in Fig. B1. Suppose an FRB is detected at position θ_{FRB} away from the beam centre, and came from a distance D_{FRB}; where it could have been detected out to a distance $D_{max}(\theta_{FRB})$ at that position in beam.

Since the beam sensitivity varies with position on the sky, the event at distance D_{FRB} would have been detectable at any point in the beam between the beam centre ($\theta = 0$) and some maximum angle θ_{max}. However, it could have been detected at a maximum distance $D_{max}(\theta)$ that varies with beam angle θ. Therefore, the total volume V_{max} in which the FRB could have been detected is the region contained beneath the $D_{max}(\theta)$ curve, while the volume V in which it was detected is the same region, albeit limited by the actual distance to the event, D_{FRB}.

It is interesting to compare the results of the integral method with that of the differential method, where V and V_{max} depend only on the values D_{FRB} and $D_{max}(\theta_{FRB})$ at the point θ_{FRB} – the point at which the FRB was detected. Clearly, for any given event, the value V/V_{max} will be different between the two methods. Yet, statistically, they give identical results.

We have tested the differential and integral methods using a simple simulation of FRBs distributed in a Euclidean space viewed by a 2-dimensional Gaussian beamshape. We generated a sample of 10^6 FRBs uniformly in the sensitive volume, and calculated V/V_{max} for each simulated FRB using both methods. In both cases a uniform distribution of V/V_{max} over the range $[0, 1]$ was obtained within statistical errors.

Appendix B.2. Time-varying Sensitivity

Time-variation of survey sensitivity, $F_{\nu,\mathrm{cutoff}}$, is no different to variation over a beam pattern – it is just another dimension. Analogously, a transients survey is characterised not just by the survey area, $\Delta\Omega$, and threshold, $F_{\nu,\mathrm{cutoff}}$, it is also characterised by its duration, T_{obs}. Likewise, the instantaneous volume element of the Universe in which transients occur is $d\Omega dz d\tau$, where proper time, $d\tau$, is simply another dimension of the volume.

Furthermore, the sensitivity of FRB surveys can also vary with time, either on rapid timescales (e.g. due to RFI) or on slow timescales (e.g. due to varying telescope configurations). The latter is a particular problem for commensal observations.

The differential and integral methods discussed above therefore apply identically to the time dimension. The differential method requires knowing the survey sensitivity only at the time of detection, whereas the integral method requires knowing the survey sensitivity for the entire duration of the survey, and integrating the volumes $V(t)$ and $V_{\mathrm{max}}(t)$ over survey time, t.

Appendix B.3. Application to the Current Work

Holographic observations have allowed accurate measurements of ASKAP's beamshape (James et al. 2019) to be made, allowing the integral method to be used to account for ASKAP's spatial variation in sensitivity over $\Delta\Omega$. However, a proper accounting of changing detector conditions with time makes the integral method too complex to deal with this dimension; we therefore use the differential method in the time domain for our analysis, by taking the survey conditions at the instant at which each FRB has been detected.

Appendix C. Error calculations for the luminosity function

The luminosity histogram is built by summing the inverse values of V_{max}. Treating this process as a weighted sum produces an error corresponding to C

$$\sigma_\nu = \sqrt{\sum_{i=1}^{N} \frac{1}{(V^i_{\mathrm{max}})^2}}, \tag{A3}$$

for N FRBs in a histogram bin. Equivalently, we can use resampling – replacing each FRB with M copies of itself, where M is an integer sampled from a Poissonian distribution of mean unity – to estimate the error. These methods produce statistically identical estimates of σ_ν. However, both formally treat the problem of 'if the observation is the truth, what is the plausible range of alternate observations?' rather than the inverse 'what range of plausible truths could reproduce this observation?'. While the latter formulation is formally correct, for many statistical problems, the difference between these two statements is small. Here, however, different values of beam efficiency B, and sparse histogram binning, lead to V_{max} varying by up to a factor of 300 within a given bin, so that individual samples dominate, and the effective sample size approaches unity. This then leads to the uncertainty in that bin being comparable to the value in the bin itself, which is a clear miscalculation of the error.

To estimate the error in each luminosity function bin therefore, we use the bootstrap resampling method above, but vary the expected mean of the Poissonian distribution by a factor k. We generate lower (upper) limits on each bin by finding the smallest (largest) factor k such that $0.5(1 - 0.6827) = 15.865\%$ of resampled values are greater than (less than) the measured value. The lower (upper) bound then becomes that bin value multiplied by k. For this purpose, we use 10^4 resamplings per bin.

https://doi.org/10.1017/pasa.2024.114 Published online by Cambridge University Press